Geochimica et Cosmochimica Acta 400 (2025) 227–247

Contents lists available at ScienceDirect

Geochimica et Cosmochimica Acta

journal homepage: www.elsevier.com/locate/gca

Mineral phases and growth conditions of morphologically diverse shelfal ferromanganese concretions

Joonas Wasiljeff [a,*], Changxun Yu [b,c], Pasi Heikkilä [a], Yann Lahaye [a,1], Matti Kurhila [a], Wei-Li Hong [d,e], Aivo Lepland [f,g,h], Sten Suuroja [h], Volker Liebetrau [i,1], Joonas J. Virtasalo [a]

[a] Geological Survey of Finland (GTK), Espoo, Finland
[b] Department of Biology and Environmental Science, Linnaeus University, Kalmar, Sweden
[c] Centre for the Environment (CENWIN), Linnaeus University, Kalmar, Sweden
[d] Department of Geological Sciences, Stockholm University, Stockholm, Sweden
[e] Baltic Sea Centre, Stockholm University, Stockholm, Sweden
[f] Department of Geology, Tallinn University of Technology, Tallinn, Estonia
[g] Geological Survey of Norway, Trondheim, Norway
[h] Geological Survey of Estonia, Rakvere, Estonia
[i] GEOMAR Helmholtz Centre for Ocean Research Kiel, Kiel, Germany

ARTICLE INFO

Associate editor: Nicholas J. Tosca

Keywords:
Ferromanganese minerals
Diagenetic redistribution
Shelf sea
Stable lead isotopes

ABSTRACT

Ferromanganese concretions in the shelf sea regions, such as the Baltic Sea, are of significant interest due to their geochemical properties, economic resource potential, and roles in benthic ecosystems. This study analyses the authigenic and detrital mineral phases and their provenance in the Baltic Sea concretions, as well as their formation mechanisms and diagenetic evolution. These concretions exist in three distinct morphotypes: crust, discoidal, and spheroidal. Using synchrotron-based techniques (μ-XRF and μ-XAS) paired with XRD, stable Pb isotope, and bulk geochemical analyses, we found that discoidal and spheroidal concretions consist of alternating Fe- and Mn-rich layers, whereas crust concretions are predominantly Fe-rich. The Mn phases primarily consist of birnessite-like phyllomanganates with columnar and branched dendritic growth patterns, indicative of microbially-mediated precipitation. In contrast, the Fe phases are represented by poorly crystalline ferrihydrite, the formation of which is influenced by admixing of detrital minerals. The three main components (Fe-rich, Mn-rich and detrital), each exhibit distinct trace element associations. The geochemical composition and morphology of the Baltic Sea concretions resembles other shelfal precipitates, indicating consistency in formation mechanisms across different shelf environments. Slightly negative to intermediate Ce anomaly values and the range in Nd contents in the samples suggest that early diagenetic processes contribute to the formation of all the morphotypes.

The lateral distribution and morphology of concretions are influenced by local hydrodynamic conditions, sedimentation dynamics, and redox fluctuations. An important factor is the periodic cover of a very organic-rich "fluffy" mud layer, which is driven by near-bottom currents, imports detrital minerals and modifies redox conditions, impacting microbial activity within the concretions. The higher occurrence of detrital minerals in Fe-rich concretions, particularly in the crust morphotype, suggests formation under stronger terrigenous influence in high-energy sedimentation conditions as opposed to more Mn containing concretions (mainly discoidal and spheroidal) forming in a relatively tranquil depositional setting and deeper water. The maturity of the detrital mineral fraction generally increases from crust to discoidal to spheroidal concretions. The Fe-rich concretions contain greater proportion of micas, clay minerals and K-feldspar to plagioclase, while the more Mn-containing concretions have proportionally high quartz contents. The detrital minerals likely act as nucleation sites promoting Fe precipitation and are redistributed diagenetically toward the interfaces dominated by Fe phases, which are slightly more tolerant to reductive dissolution than Mn phases. The preferential reductive dissolution of Mn phases results in thick Fe-rich growth layers and relative enrichment of the detrital mineral fraction. Stable Pb isotope data show distinct regional signatures, indicating that the composition of concretions is affected by

* Corresponding author.
E-mail address: joonas.wasiljeff@gtk.fi (J. Wasiljeff).
[1] Deceased.

https://doi.org/10.1016/j.gca.2025.05.012
Received 6 October 2024; Accepted 8 May 2025
Available online 12 May 2025

bedrock erosion in the catchment area. Our findings highlight contrasts in mineral phases, geochemistry, formation environments, and diagenetic evolution across sites in Fe-rich crust concretions compared to more Mn containing discoidal and spheroidal concretions. These insights are relevant to ferromanganese concretions in shelf areas worldwide, and their potential use in paleoenvironmental reconstructions and resource exploration.

1. Introduction

Ferromanganese concretions are biogeochemical precipitates that are of broad interest due to their potential as resources of economically important elements, their contribution to benthic food-web integrity, their function as paleoenvironmental archives, and their role in dark oxygen production in the deep sea (Hein et al., 2020; Stratmann et al., 2021; Park et al., 2023; Sweetman et al., 2024). These precipitates are widely distributed across oceans and shelf areas worldwide (Baturin, 2010, 2019; González et al., 2010; Zhamoida et al., 2017; Zhong et al., 2017; Vereshchagin et al., 2019). The formation of shelfal ferromanganese concretions, such as those found in the Baltic Sea, usually occurs in seafloor areas that are well oxygenated with low sediment deposition and organic matter delivery rates, and where colloidal iron (Fe) and manganese (Mn) oxyhydroxides are supplied from surrounding catchment areas or nearby anoxic seafloor sediments through diagenetic remobilization (Ingri and Pontér, 1986; Marcus et al., 2004; Winterhalter, 2004; Zhamoida et al., 2007). These concretions are efficient at scavenging trace metals including rare-earth elements (REEs) from the seawater, increasing their economic importance. The elemental composition and distribution of metals in ferromanganese concretions are mainly governed by phase-related interactions and intricate elemental complexations (Huang and Fu, 2023; Ren et al., 2024a). These interactions are driven by the electro-affinities of the elements to binding phases. The formation of ferromanganese mineral phases is mainly affected by metal fluxes and the environmental redox potential (Glasby et al., 1997), the latter being influenced by factors such as sedimentation rate, circulation patterns of water masses, and organic carbon accumulation (Glasby, 1972; Glasby et al., 1997). These factors depend on the water depth and biological productivity in the surface waters. Additionally, the variable supply of organic matter, combined with bioturbation and the physical mixing of sediments by near-bottom currents, as well as microbial activity, result in fluctuating redox conditions in the sediments and porewater, affecting the incorporation of elements into the concretions (Shulga et al., 2022). Typically, the Fe and Mn phases in concretions are poorly crystalline, containing amorphous Fe-Mn oxyhydroxides and minerals such as ferrihydrite and birnessite (e.g. Post, 1999; Marcus et al., 2004; Baturin, 2009).

In addition to the elemental composition and mineralogy, also the occurrence and morphology of shelfal ferromanganese concretions have been the focus of several studies over the past few decades. Many of these deposits occur in near-shore environments in water depths of less than 200 m in regions such as the Kara Sea, Black Sea, and the Baltic Sea (Kaikkonen and Virtanen, 2022). In the Baltic Sea, the concretions cover ca. 10 % of the sea floor at depths of 20–100 m (Glasby et al., 1997; Kaikkonen et al., 2019), and may be intermittently covered by a thin layer of "fluffy" very organic-rich mud (Zhamoida et al., 2017). They are commonly located along the peripheries of major seafloor depressions (Glasby et al., 1997), whereas shallower areas have sporadic occurrences predominantly at locations where sediments that accumulated during the glaciolacustrine and post-glacial lacustrine phases of the Baltic Sea evolution are exposed on the seafloor (Zhamoida et al., 2007, 2017). Terrigenous input from river discharge is considered as a significant source of Fe and Mn for the concretion formation in the Baltic Sea (Winterhalter, 1980; Zhamoida et al., 1996). Another major source of Mn and Fe is the glacial till originating from Precambrian Baltic Shield crystalline rocks (Callender and Bowser, 1976). Glaciolacustrine rhythmites (varved clays) and post-glacial lacustrine clays, which cover the crystalline bedrock and till, are characterized by elevated reactive Mn and Fe contents and can serve as Mn and Fe sources (Virtasalo and Kotilainen, 2008). Concretion abundance and Mn/Fe ratio typically increase with depth due to the greater Mn mobility compared to Fe in anoxic environments of the deepest basins (Force and Cannon, 1988; Huckriede and Meischner, 1996; Lenz et al., 2015).

In the Baltic Sea, ferromanganese concretions are porous, and three endmember morphotypes (crust, discoidal, and spheroidal) have been recognized (Zhamoida et al., 1996; Winterhalter, 2004; Wasiljeff et al., 2024a). Similar morphologies have been observed in concretions found from other shelf sea regions, such as the Kara Sea and Black Sea (Baturin, 2010; Vereshchagin et al., 2019), suggesting common formation mechanisms across these environments. It has been suggested that the formation of different morphotypes is influenced by hydrodynamic and sediment depositional conditions in the near-bottom environment, and the concretion's position within the sediment (Glasby et al., 1997; Shulga et al., 2022; Wasiljeff et al., 2024a). Yet, the precise mechanisms regulating the metal contents and morphology of the concretions remain poorly constrained. It is known that the concretions serve as habitats for abundant and diverse microbial communities, which can regulate their nutrient and metal cycling (Ghiorse and Hirsch, 1982; Zhang et al., 2002; Yli-Hemminki et al., 2014; Reunamo et al., 2017). Microbial biomineralization seems to be most efficient in the discoidal and spheroidal morphotypes (Wasiljeff et al., 2024a; Majamäki et al., 2025). The growth rates of concretions in the Baltic Sea are notably high, in the range of micrometers per year (Liebetrau et al., 2002, 2004; Anufriev and Boltenkov, 2007; Grigoriev et al., 2013; Majamäki et al., 2025), when compared to a few millimeters per million years on the deep ocean floor (e.g. Frank et al., 1999; Klemm et al., 2005; Marcus et al., 2015). The rapid growth is consistent with microbial catalysis of their formation.

Shelfal ferromanganese concretions are typically impure and contain variable amounts of accessory detrital mineral phases (e.g. Hein et al., 2017; Baturin, 2019). However, the composition and origin of detrital components have not been thoroughly addressed in previous studies. The mineralogical and geochemical characteristics of detrital phases are determined by the source rock composition, current weathering environment, sediment recycling and, hydrodynamic sorting during transport. Moreover, the diagenetic alteration at the deposition site, involving dissolution and reprecipitation cycles of the ferromanganese concretions, could potentially rearrange the detrital mineral distribution and composition in a concretion by compaction and selective phase dissolution.

Stable Pb isotopic ratios ($^{206,\ 207,\ 208}Pb/^{204}Pb$) are commonly utilized tools in provenance studies of marine ferromanganese concretions (Frank, 2002; Liebetrau et al., 2004; Ling et al., 2005; Goto et al., 2017; Josso et al., 2020a; Zhang et al., 2025). These isotopes provide a multidimensional approach that is not significantly fractionated by natural processes such as chemical weathering, biological fractionation, phosphatization events, or diagenesis in the concretions (Ling et al., 2005). The Pb isotopic composition is mainly influenced by continental input and hydrothermal solutions (Frank, 2002). In the Baltic Sea, where hydrothermal inputs are not expected, the Pb isotopic composition reflects the continental input, making them a powerful tool for assessing the provenance of the concretion source material.

This study presents a detailed analysis of mineral phases, authigenic mineral phase forming mechanisms, and the provenance of concretion-forming materials in morphologically diverse ferromanganese concretions from the Baltic Sea, aiming to increase the understanding of the broader processes governing growth and diagenetic evolution of shelfal

concretions. The analysis is based on elemental contents and ratios, synchrotron-based μ-X-ray fluorescence (μ-XRF) mapping paired with μ-X-ray absorption spectroscopy (μ-XAS) results, mineralogical characterizations with bulk sample powder X-ray diffraction (XRD), and stable Pb isotope data of a sample set of ferromanganese concretions from the major northern sub-basins and from the Mecklenburg Bight in the southern Baltic Sea. The commonly applied bulk geochemical and mineralogical analyses in aquatic ferromanganese concretion studies (e.g. Bau et al., 2014; Josso et al., 2017; Dekov et al., 2021) cannot resolve intricate microscale phase-associations of these heterogenous precipitates (Ren et al., 2024b). Such a limitation justifies our combined strategy of the *in-situ* mineralogical characterization, elemental mapping, and statistical analysis of the bulk geochemistry to infer elemental associations and their relationship with the complex growth environments of shelfal ferromanganese concretions.

2. Samples and methods

2.1. Study area

In this study we investigated the northern Baltic Sea (Gulf of Bothnia), the north-eastern Baltic Sea (Archipelago Sea and Gulf of Finland) as well as the southwestern Baltic Sea (Mecklenburg Bight).The bedrock of the north–north-eastern part of the study region consists of Paleoproterozoic crystalline basement of mainly granitoid rocks that crop out locally on the seafloor, as well as of Mesoproterozoic and Cambrian and Ordovician sedimentary rocks in tectonic depressions in the Gulf of Bothnia (Koistinen et al., 2001). The Baltic Sea Basin has been overdeepened by erosion during multiple glaciations, lastly by the Fennoscandian continental ice sheet during the Late Weichselian (Late Pleistocene). The northwestward retreat of the ice-sheet margin from the eastern Gulf of Finland began ca. 13 500 calendar years ago, from the Archipelago Sea 11 600 years ago, and from the Bothnian Bay 10 300 years ago (Sauramo, 1929; Saarnisto and Saarinen, 2001; Stroeven et al., 2016). The retreating ice-margin left behind till and glacial outwash deposits in a deep and large ice-contact lake, where glaciolacustrine varved silt and clay, and successive post-glacial lacustrine weakly layered silty clay, were deposited as conformable drapes of comparably uniform thickness of several meters (Virtasalo et al., 2007, 2014). Beginning at ca. 7600 years ago, the thresholds to the Atlantic in the Kattegat were inundated due to the glacioeustatic sea-level rise, resulting in the establishment of brackish-water conditions and drift-type deposition of organic-rich mud. Sediment distribution on the present seafloor is patchy; roughly a third is composed of bedrock and till, a third of glaciolacustrine and postglacial lacustrine silty clay, and a third of ongoing accumulation of organic-rich brackish-water mud. The ferromanganese concretions typically rest on the exposed lacustrine silty clays and encrust till and glaciofluvial stones (Winterhalter, 2004).

The Mecklenburg Bight in the southwestern Baltic Sea was deglaciated already 17 000 years ago (Stroeven et al., 2016). The bedrock in this region predominantly consists of Paleogene deposits (Lüthgens et al., 2020). Ferromanganese concretions found in this area typically

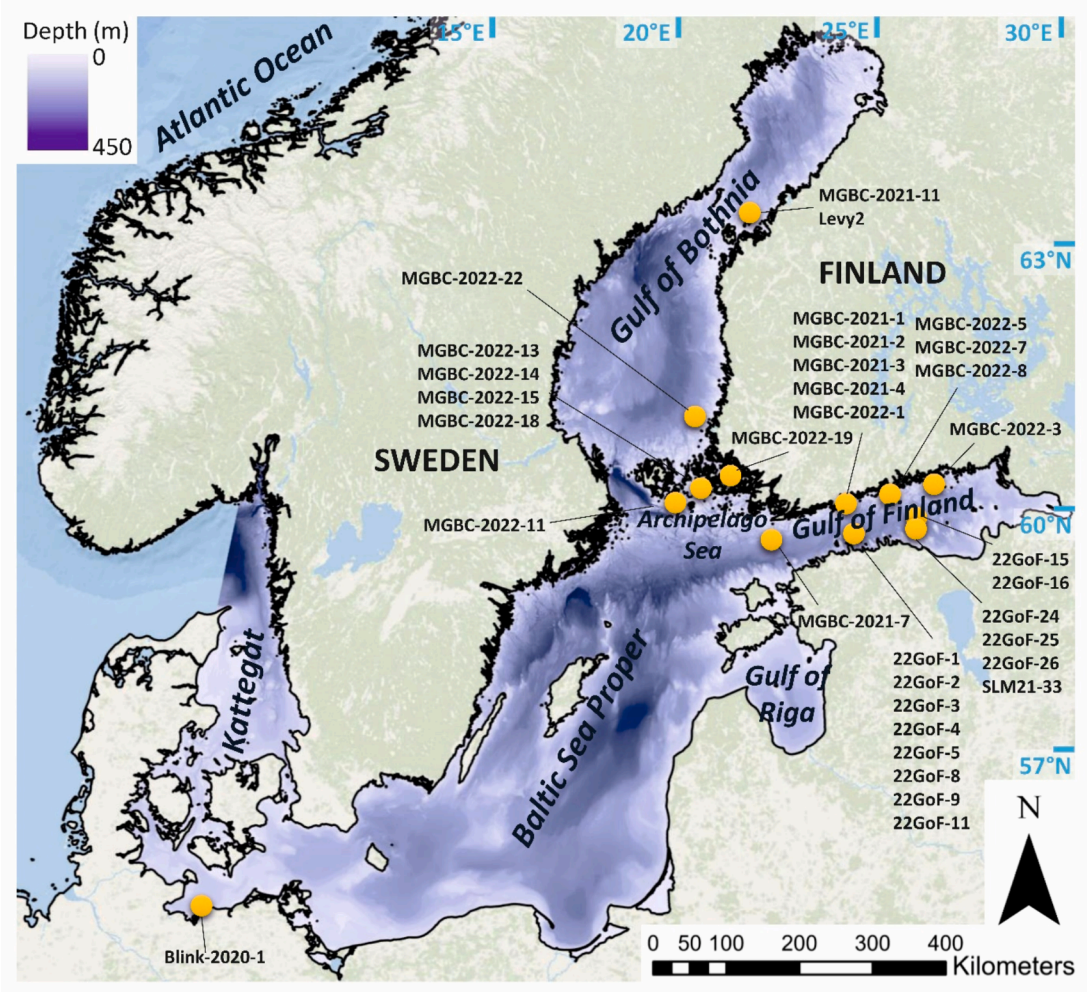

Fig. 1. Approximate sampling locations in the Baltic Sea. Base map: ESRI Inc. (Redlands) Ocean Basemap 2018. Baltic Sea bathymetric data: EMODnet Bathymetry 2018 (Thierry et al., 2019).

have discoidal shapes or encrust exposed till stones (Glasby et al., 1997).

2.2. Sample collection

Ferromanganese concretions of diverse size and morphology were collected in 2021 and 2022 during expeditions onboard r/v *Geomari* (Geological Survey of Finland, GTK) and r/v *Electra* (Stockholm University) to the eastern and western Gulf of Finland, the Archipelago Sea, and the Gulf of Bothnia (Fig. 1). The concretion samples were collected using a box corer onboard *Geomari* or both grab sampler and a short Gemax gravity corer onboard *Electra*. The samples collected onboard *Geomari* were immediately flushed throughout with ultra-pure water and frozen using dry ice, while the *Electra* samples were stored in cool conditions. All samples were freeze-dried at the GTK laboratory. In addition, sample slices were collected at 1 cm vertical intervals of the sediment underlying the concretions for geochemical analyses. From this collection, representative ferromanganese concretions of the three main morphotypes in the Baltic Sea, namely crust, discoidal, spheroidal were selected for further analysis (Table 1).

2.3. Methods

Thin-sections were prepared for mapping the micro-scale distribution of Fe and Mn and mineralogy in three selected concretions of different morphotypes using the BioXAS-imaging beamline *(07ID-1)* at the Canadian Light Source (CLS), Saskatchewan, Canada. μ-XRF maps of Fe and Mn were obtained by raster scanning the concretion samples under a monochromatic beam with an energy of 7.2 or 7.5 keV, a size of

Table 1
Morphotypes, collection locations, water depths, and morphotypes of the studied ferromanganese samples.

Sample	Morphotype	Location	Lat (N)	Lon (E)	Depth (m)
MGBC-2022-11_Lab1	Crust	AS	59°53.342	20°44.947	41.0
MGBC-2022-11_Lab2	Crust	AS	59°53.342	20°44.947	41.0
MGBC-2022-13_Lab1	Crust	AS	60°05.569	21°16.312	51.0
MGBC-2022-13_Lab2	Crust	AS	60°05.569	21°16.312	51.0
MGBC-2022-19_Lab1	Crust	AS	60°16.944	22°00.285	37.0
MGBC-2022-19_Lab2	Crust	AS	60°16.944	22°00.285	37.0
MGBC-2022-14-C-L1	Crust	AS	60°05.916	21°19.700	36.0
MGBC-2022-14-C-L2	Crust	AS	60°05.916	21°19.700	36.0
Levy2[a,b]	Crust	GoB	63°33.747	21°54.616	32.2
MGBC-2022-22_Lab1	Crust	GoB	61°12.612	21°04.353	46.0
MGBC-2021-11-C-L1	Crust	GoB	63°33.747	21°54.616	32.2
MGBC-2021-11-C-L2	Crust	GoB	63°33.747	21°54.616	32.2
MGBC-2022-1_Lab1	Crust	GoF	59°57.941	24°46.718	45.2
MGBC-2022-1_Lab1 (2)	Crust	GoF	59°57.941	24°46.718	45.2
22GoF-15_Lab1	Crust	GoF	59°55.034	26°20.523	80.0
22GoF-24_Lab1	Crust	GoF	59°49.020	26°12.600	60.0
22GoF-25_Lab1	Crust	GoF	59°49.020	26°12.600	60.0
22GoF-26_Lab1	Crust	GoF	59°49.020	26°12.600	60.0
MGBC-2021-4-1-B[b]	Crust	GoF	59°57.929	24°46.726	45.4
MGBC-2021-4-C-L1	Crust	GoF	59°57.929	24°46.726	45.4
MGBC-2021-7-C-1	Crust	GoF	59°38.245	23°19.928	54.4
MGBC-2022_18_Lab1	Discoidal	AS	60°02.746	21°35.102	18.0
MGBC-2022-15-D-L1	Discoidal	AS	59°59.891	21°39.648	26.0
MGBC-2022-15-D-L2	Discoidal	AS	59°59.891	21°39.648	26.0
MGBC-2022-18-D-L2	Discoidal	AS	60°02.746	21°35.102	18.0
MGBC-2022-3_Lab1	Discoidal	GoF	60°17.413	26°48.355	36.0
MGBC-2022-3_Lab2	Discoidal	GoF	60°17.413	26°48.355	36.0
MGBC-2022-5_Lab1	Discoidal	GoF	60°11.483	26°01.895	29.0
MGBC-2022-5_Lab2	Discoidal	GoF	60°11.483	26°01.895	29.0
22GoF-1_Lab1	Discoidal	GoF	59°43.400	24°53.548	94.0
22GoF-2_Lab1	Discoidal	GoF	59°43.460	24°53.587	90.0
22GoF-4_Lab1	Discoidal	GoF	59°43.593	24°53.552	88.0
22GoF-5_Lab1	Discoidal	GoF	59°43.649	24°53.597	80.0
22GoF-11_Lab1	Discoidal	GoF	59°43.484	24°53.615	91.0
MGBC-2021-1-D-L1	Discoidal	GoF	60°03.907	24°44.320	23.2
22GoF-4-D-L2	Discoidal	GoF	59°43.593	24°53.552	88.0
Blink-2020-1a[b]	Discoidal	MB	54°10.100	11°21.000	~20
SLM21-33-D-1[a]	Discoidal	GoF	59°40.470	26°33.120	30.8
MGBC-2022-7_Lab1	Spheroidal	GoF	60°05.493	25°57.789	44.0
MGBC-2022-7_Lab2	Spheroidal	GoF	60°05.493	25°57.789	44.0
MGBC-2022-8_Lab1	Spheroidal	GoF	60°01.000	26°04.812	60.0
MGBC-2022-8_Lab2	Spheroidal	GoF	60°01.000	26°04.812	60.0
22GoF-8_Lab1	Spheroidal	GoF	59°43.510	24°53.570	95.0
22GoF-9_Lab1	Spheroidal	GoF	59°43.534	24°53.662	95.0
22GoF-16_Lab1	Spheroidal	GoF	59°55.110	26°20.537	80.0
MGBC-2021-2-S-L1	Spheroidal	GoF	59°57.591	24°46.101	57.2
MGBC-2021-2-S-L2	Spheroidal	GoF	59°57.591	24°46.101	57.2
MGBC-2021-2-S-T3[a]	Spheroidal	GoF	59°57.591	24°46.101	57.2
MGBC-2021-3-S-L1	Spheroidal	GoF	59°57.846	24°46.440	50.9
MGBC-2021-3-S-L1_2	Spheroidal	GoF	59°57.846	24°46.440	50.9
MGBC-2021-3-S-L2	Spheroidal	GoF	59°57.846	24°46.440	50.9
MGBC-2021-3-S-L3	Spheroidal	GoF	59°57.846	24°46.440	50.9
MGBC-2022-7-S-L3	Spheroidal	GoF	60°05.493	25°57.789	44.0

AS = Archipelago Sea, GoB = Gulf of Bothnia, GoF = Gulf of Finland, MB = Mecklenburg Bight.
[a] = synchrotron μ-XRF mapping and μ-XAS point analyses.
[b] = stable Pb isotope analyses.

5 × 5 μm or 6 × 6 μm, and a dwell time of 100 ms. The XRF yields were recorded by a 4-element Vortex detector that was posited at 45 degrees relative to the incident beam. The μ-XRF data were treated and analyzed using the PyMca software (Solé et al., 2007). On selected points, Fe and/or Mn X-ray absorption near edge structure (XANES) and extended X-ray absorption fine structure (EXAFS) spectra were recorded in fluorescence mode by scanning from −150 eV to +7.5–10.5 *k* ($Å^{-1}$), relative to the Fe and Mn K-edges, respectively, at step sizes of 5 eV from −100 to −50 eV, 0.5 eV from −50 to +50 eV, and 0.05 $Å^{-1}$ from +50 eV to +7.5–10.5 *k*. The spectra were processed following the standard procedures (e.g., background subtraction, and normalization) using the Athena software (Ravel and Newville, 2005).

The identification of crystalline phases was done by X-ray powder diffraction (XRD, XRPD) at the GTK Espoo research laboratory. Samples were prepared by powdering 70 mg of each sample in agate mortar in acetone suspension that was poured on zero-background holder, spread equally and dried. The samples were measured using a D8 Discover (Bruker, USA) Bragg-Brentano powder diffractometer equipped with Cu-tube, automatic divergence slits, 2.5° soller slits, motorized anti-scatter screen (MASS), spinner, and LYNXEYE XE-T silicon strip detector. Powder diffractograms were measured from a 4–110° 2θ range using 40 kV and 40 mA power settings in continuous mode, 0.02 °2θ/s for 1.5 h/sample. Phase identifications were carried out with Bruker EVA software and ICDD (International Centre for Diffraction Data) PDF-4 (Powder Diffraction File) Minerals 2024 database.

The Rietveld refinements were done using Malvern Panalytical HighScore Plus 4.9. Due to the complications by several poorly crystalline and amorphous phases present in these samples, the refinement required several stages. First, the phase assemblage was developed by refining each phase from the sample where it is the most dominant, and Partially Or No Known Crystal Structure (PONKCS) refinement phase (Scarlett and Madsen, 2006) was used to stabilize the amorphous background. The refinement parameters used include scale factors, Chebyshev 1 background polynomial, unit cell parameters, Pseudo Voigt Caglioti peak profile functions, March Dollase preferred orientation, and some site occupancy factors. Brindley micro-absorption correction was used to compensate the absorption of the Cu-tube signal to Fe-bearing phases with average particle diameter of 5 μm. In the second stage, parameter limits for each phase were selected by iterating batch refinements of automatic fitting sequences until the same phase assemblage was stable for all samples. Finally, details in each sample were manually refined for a better fit of residual weighed parameter (Rwp) < 8. The results were validated by comparing XRD Rietveld back calculated bulk chemical composition with ICP-OES four-acid digestion results (see below): positive correlation was found for all major elements. The phase composition results are considered semi-quantitative and used only graphically to observe relative differences between concretion morphologies.

Scanning electron microscope (SEM) imaging was carried out with a JEOL JSM-7100F (JEOL Ltd., Japan) Schottky Field Emission Scanning Electron Microscope (FE-SEM) equipped with an Oxford Instruments EDS-spectrometer X-Max 80 mm^2 (SDD) at 20 kV acceleration voltage and a 1.3nA probe current at the GTK.

The multi-element chemical compositions of the bulk concretion samples and sediment samples were measured at Eurofins Labtium, Finland: As, Be, Bi, Cd, Co, Mo, Pb, Rb, Sb, Sc, Sn, Th, U, W, Hf, Y, Nb, Zr, and REEs were determined by inductively coupled plasma mass spectrometry (ICP-MS) whereas Al, Ba, Ca, Cr, Cu, Fe, K, Mg, Mn, Na, Ni, P, S, Sr, Ti, V and Zn were determined by inductively coupled plasma atomic emission spectroscopy (ICP-OES) after sample digestion with a combination of nitric, perchloric, and hydrofluoric acid with a final dissolution stage with hydrochloric acid (four-acid digestion).

Pb isotopes (^{208}Pb, ^{207}Pb, ^{206}Pb and ^{204}Pb) were determined with laser ablation (LA)-ICP-MS using a Nu Instruments AttoM (Nu Instruments Ltd, UK) single collector high resolution (SC-HR)-ICP-MS coupled with a New Wave (New Wave Research Inc., USA) solid state deep UV (193 nm) laser at the GTK. Laser operating conditions were 10 Hz rep rate, and 2.9 J cm^{-2} fluence. Data were acquired with time resolved analysis (TRA) in transects using 25 μm spots where ablation spots were lined perpendicular to concretion growth axis. Each line was split after acquisition of 250 μm. Isotope values were corrected using standard bracketing to NIST610. Quality control standard (USGS Nod-P-1) was measured in the same session before and after each set of unknowns. Values for ^{204}Pb were corrected for interference of the ^{204}Hg using ^{202}Hg.

Rare-earth element and yttrium (REY) plots were normalized to Post-Archean Australian Shale (PAAS) (Pourmand et al., 2012) and to average values of the Baltic Sea floor surface sediments from concretion sampling locations (Wasiljeff et al., 2024b). Cerium anomaly (Ce/Ce* ratio) was defined as:

$$Ce/Ce^{*} = 2Ce_N/(La_N + Pr_N) \quad (1)$$

where the subscript N indicates normalization to PAAS (Pourmand et al., 2012). The Pearson correlation coefficient was employed to compute matrices for the chemical data, assessing the degree of linear dependence between pairs of variables, utilizing Origin Pro 2024b software (version 10.1.5.132).

3. Results

3.1. Mineralogy

The μ-XRF elemental maps of Fe and Mn show that the discoidal and spheroidal ferromanganese concretions from the Baltic Sea primarily consist of alternating growth layers of Fe- and Mn-rich phases (Fig. 2a and c). In contrast, crust concretions were predominantly composed of Fe-rich phases (Fig. 2b).

The Mn and Fe XANES and EXAFS spectra for most of the selected points were similar, indicating that the studied concretions, irrespective of morphotype (crust, discoidal, and spheroidal) and sampling depth, contained similar Fe and Mn phases (Fig. 3a–d). In Mn-rich layers, the Mn XANES and EXAFS spectra mainly followed those of three phyllomanganate references (hexagonal birnessite, triclinic birnessite and vernadite), while in the Fe-rich layers, the predominant Fe phase was most likely 2-line ferrihydrite (Fig. 3). Fe was present also in Mn-rich layers, and Mn was present in Fe-rich layers. Our XANES and EXAFS data showed that the accessory Fe-phase in Mn-rich layers is similar to 2-L ferrihydrite, whereas the Mn-containing accessory phase in Fe-rich layers was dominated by either Mn(II)-sorbed ferrihydrite or Mn(III) hydroxides (e.g., manganite or feitknechtite).

The XRD data of the ferromanganese concretions show complex distribution of diffraction peaks. These can be classified into sharp reflections of the detrital mineral phases, and broad, shallow peaks accompanied by elevated background areas of X-ray amorphous, poorly crystalline, and nanocrystalline ferromanganese precipitates (Fig. 4). Clay minerals show intermediate diffraction properties between these endmembers. Identified detrital mineral phases comprise quartz, K-feldspar (microcline), albitic plagioclase feldspar, biotite and muscovite micas, chlorite and clinoamphibole (e.g. hornblende or tremolite-actinolite). The ferromanganese precipitates are mostly X-ray amorphous, forming two very broad background elevations centered at 2.6 Å and 1.54 Å d-spacings (35 and 60° 2-theta (Cu), respectively).

In Mn-rich concretions, the most distinct broad peaks of nanocrystalline order are at 7.15 Å, 2.45 Å (with quartz overlap), and 1.42 Å (Fig. 4). Local diffraction profile elevations can be interpreted using the combination of birnessite and vernadite. In general, the Mn-rich concretions are low in detrital mineral content, with only the main peaks of quartz, feldspars and 10 Å micas detected. The XRD patterns of Fe-rich concretions are complicated mixtures of detrital minerals, phyllosilicates, and broad peaks of nanocrystalline Fe-phases that can be interpreted as a combination of ferrihydrite and goethite. The peaks of

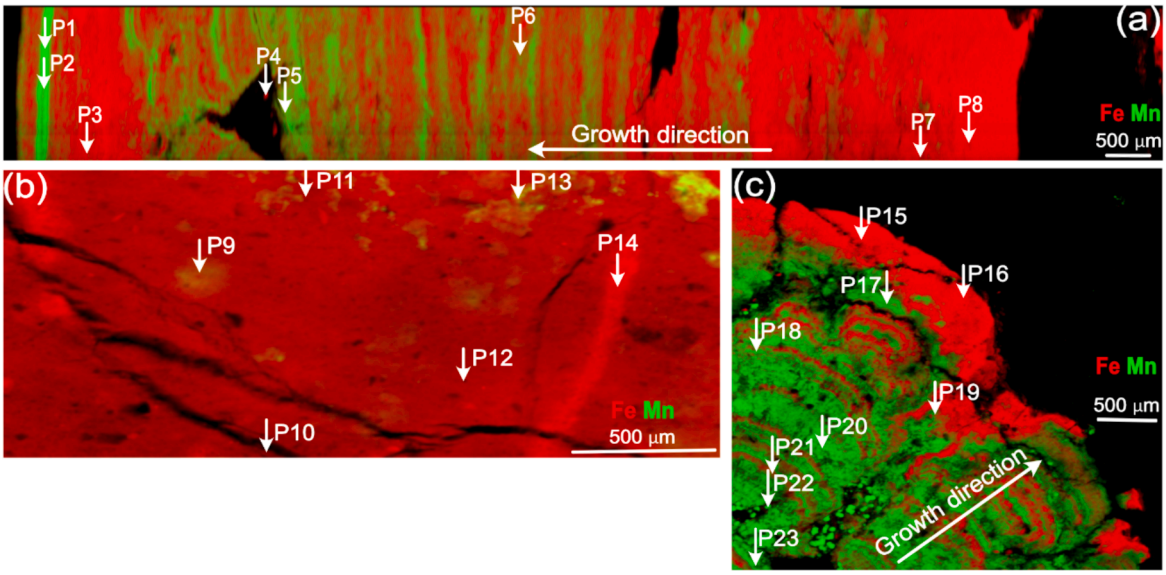

Fig. 2. Synchrotron-μ-XRF maps showing Fe (red) and Mn (green) distributions in (a) discoidal, (b) crust, and (c) spheroidal concretions from the Baltic Sea. Measured XAS data points (P1 to P23) are indicated in the Figure. The white scale bars equal 500 μm. Apparent growth directions are indicated with a white arrow.

biotite, muscovite and chlorite are distinctly broadened at the peak tails and explain some of the broad peaks at the diffractogram center, partly overlapping with potential ferrihydrite and goethite signals. Clay minerals such as kaolinite, illite and smectite were not detected in significant content. Interestingly, the Fe-rich concretions show more distinct signal of Mg-Fe-silicates biotite, chlorite and clinoamphibole than the Mn-rich concretions that contain only K-Na-Al-silicates, quartz, feldspars and muscovite/illite. The discoidal concretion sample with Mn# 0.52 [defined as atomic Mn/(Mn + Fe)] is anomalous in showing almost no signal of Fe-Mn-oxyhydroxides with crystalline detrital mineral phases dominating the mineral composition without visible amorphous background. Only one broad peak at ~7 Å indicates the potential presence of planar birnessite flakes.

The semi-quantitative Rietveld refinement bulk phase composition results show that the crust morphotype of the ferromanganese concretions is characterized by relatively enriched mica content, compared to quartz and feldspars (Fig. 5). With Mn# as low as 0.05, signals of Fe oxyhydroxides resembling goethite and ferrihydrite are recognized by the refinement. The spheroidal morphotype is low in detrital component and displays the strongest signals for Mn oxyhydroxides resembling birnessite and vernadite. The two discoidal samples show very different ratio between the detrital and ferromanganese precipitate contents. The discoidal sample with intermediate Mn# of 0.16 resembles the spheroidal morphotype in phase composition, although having lower Mn/Fe. The other discoidal sample owes the highest Mn# of the XRD studied samples (0.52). It is exceptionally high in detrital feldspars and quartz, but particularly low in micas. Of these samples, the mica content is in general inversely proportional with Mn#, i.e. slow deposition of clay-size particles is accompanied with chemical precipitates of high Fe/Mn.

The presence of various detrital mineral phases is consistent with FE-SEM observations (Fig. 6). The Fe-rich (mainly crust) concretions contain greater proportion of micas, clay minerals and K-feldspar to plagioclase, while the more Mn-containing spheroidal and discoidal concretions contain relatively higher amounts of quartz in comparison to feldspars, micas and clay minerals. The detrital minerals are often admixed with the Fe-rich layers or at the Fe-Mn layer interfaces (Fig. 6c).

3.2. Bulk geochemistry of major and trace elements

Statistics of the bulk chemical compositions of the different morphotypes are presented in Table 2 and are included in (Wasiljeff et al., 2024b). The mean Fe content of the crust concretions is 18.7 wt% (median: 19.5 %, range: 6.8–29.9 wt%), whereas discoidal concretions contain 20.0 wt% of Fe (median: 24.2 wt%, range: 3.2–35.9 wt%), and spheroidal concretions 16.4 wt% (median: 16.4 wt%, range: 6.5–24.0 wt %). Mean Mn contents for the different morphotypes are 5.0 wt% (median: 3.0 wt%, range: 0.4–16.8 wt%), 6.6 wt% (median: 5.9 wt%, range: 1.3–13.2 wt%), and 8.5 wt% (median: 8.1 wt%, range: 4.9–14.0 wt%), respectively. This results in the highest mean Fe/Mn ratios in crust concretions (mean: 13.9, median: 5.1), followed by discoidal concretions (mean: 6.94, median: 4.1) and spheroidal concretions (mean: 2.4, median: 2.0). Aluminum (Al) contents ranged between 1.1 and 7.1 wt% with crust concretions exhibiting the highest mean value of 4.3 wt%. Similarly, Ti contents were the highest in the crust morphotype (mean: 0.24 wt%), overall ranging from 0.03 to 0.47 wt% in all morphotypes.

REY distributions normalized to PAAS show that most of the samples contain negative Ce and Eu anomalies and positive Y and Gd anomalies (Fig. 7a–c). When normalized to Baltic Sea surface sediment REY contents (Fig. 7d–f), the concretions show overall enriched values, with negative Ce and Eu anomalies but subtle or no Y or Gd anomalies. The range in enrichment and depletion of REY in comparison to PAAS or Baltic Sea surface sediment is the largest in discoidal concretions, followed by crusts and spheroidal concretions.

The Pearson correlation coefficient matrix calculated for the samples (Fig. 8), alongside the XAS and XRD mineralogical data and FE-SEM observations, indicates the presence of three principal phase associations: a Fe-rich phase, a Mn-rich phase, and an Al-bearing detrital phase. These three major phases have following element associations with decreasing correlation coefficient values for each phase:

Fe-rich phase (P, HREE, Pb, As, LREE, Y, V, Be, and U)
Mn-rich phase (Ba, Sr, S, Sb, Mo, Cd, Cu, and Ni)
Al-bearing detrital phase (Ti, Nb, Sc, Rb, Th, Sn, Hf, K, Zr, V, Be, Mg, Bi, As, and Na)

3.3. Detrital component

In contrast to REEs and Y, other high field strength (HFS) elements such as Zr and Ti, as well as mobile elements like Na, K, and Mg, show either no correlation or a strong negative correlation with Fe and Mn contents, but a strong positive correlation with Al content. This suggests that these elements are primarily hosted by detrital minerals in the

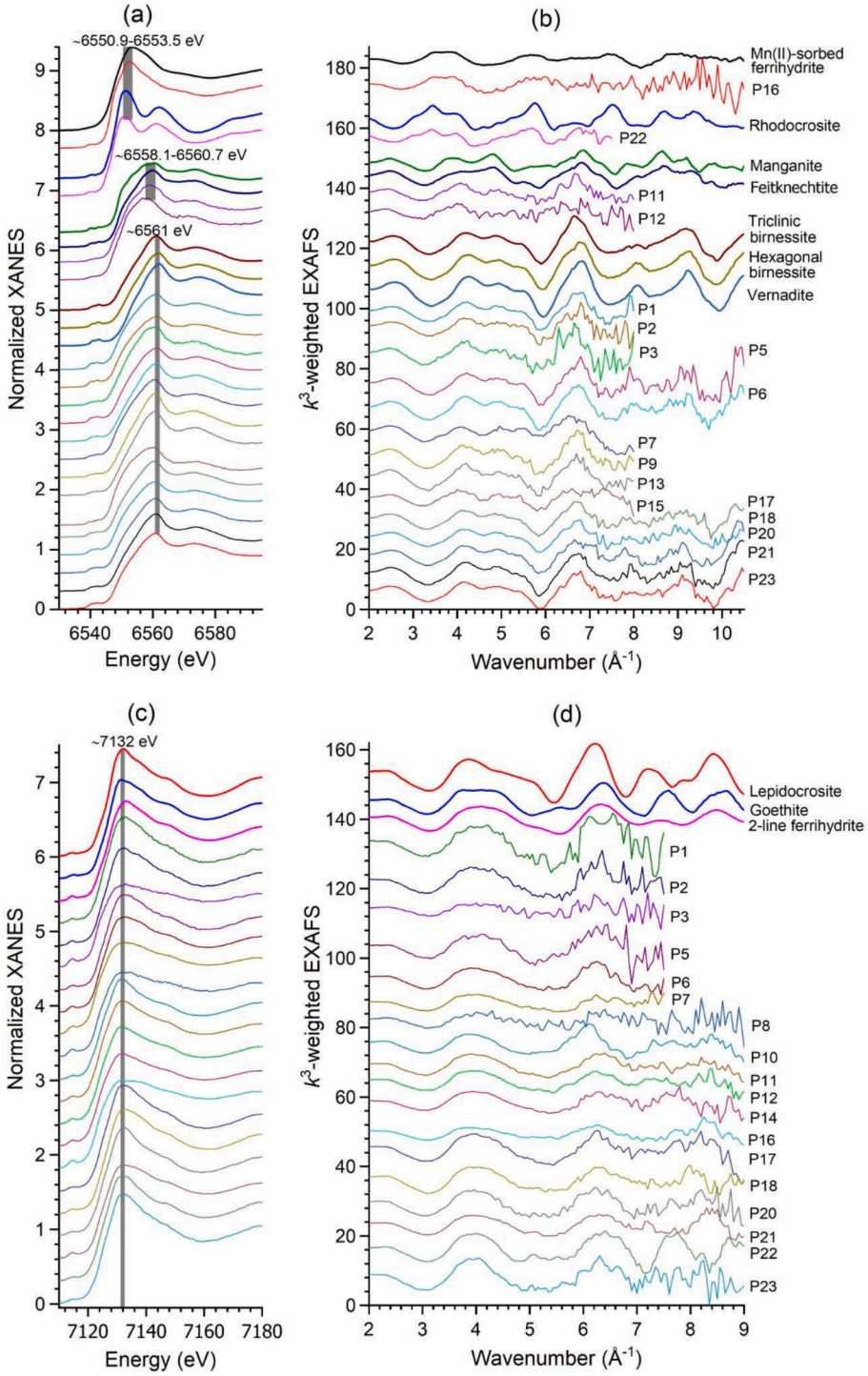

Fig. 3. Normalized (a) Mn and (c) Fe K-edge XANES and k^3-weighted (b) Mn and (d) Fe EXAFS spectra. Measured XAS data points (P1 to P23) are the same as indicated in Fig. 2.

Baltic Sea concretions.

The endmember morphotypes of the Baltic Sea ferromanganese concretions can be differentiated by their contents of detrital phase-hosted elements and present-cycle weathering products. The crust concretions exhibit the highest concentrations of Al and Ti, whereas the spheroidal concretions show the lowest concentrations of the detrital elements (Fig. 9a). The discoidal concretions typically display intermediate contents of these elements in comparison with the other morphotypes. However, Zr generally exhibits similar values across the different morphotypes. XRD measurements reveal an increased clay fraction in the Fe-rich crust concretions (Fig. 5).

Based on traditional weathering indices, the Chemical Index of Alteration (CIA = $Al_2O_3/(Al_2O_3 + Na_2O + K_2O + CaO^*) \times 100$) (Nesbitt and Young, 1982) and the Weathering Index of Parker (WIP = $(CaO^*/0.7 + 2Na_2O/0.35 + 2K_2O/0.25 + MgO/0.9) \times 100$) (Parker, 1970), the terrestrial detrital fraction in the concretions is mostly unweathered. On the other hand, XRD analyses suggest that the detrital fraction in discoidal and spheroidal concretions might have undergone more extensive sedimentary reworking based on quartz to feldspar ratios, whereas the crust concretions have increased abundance of clays, as suggested also

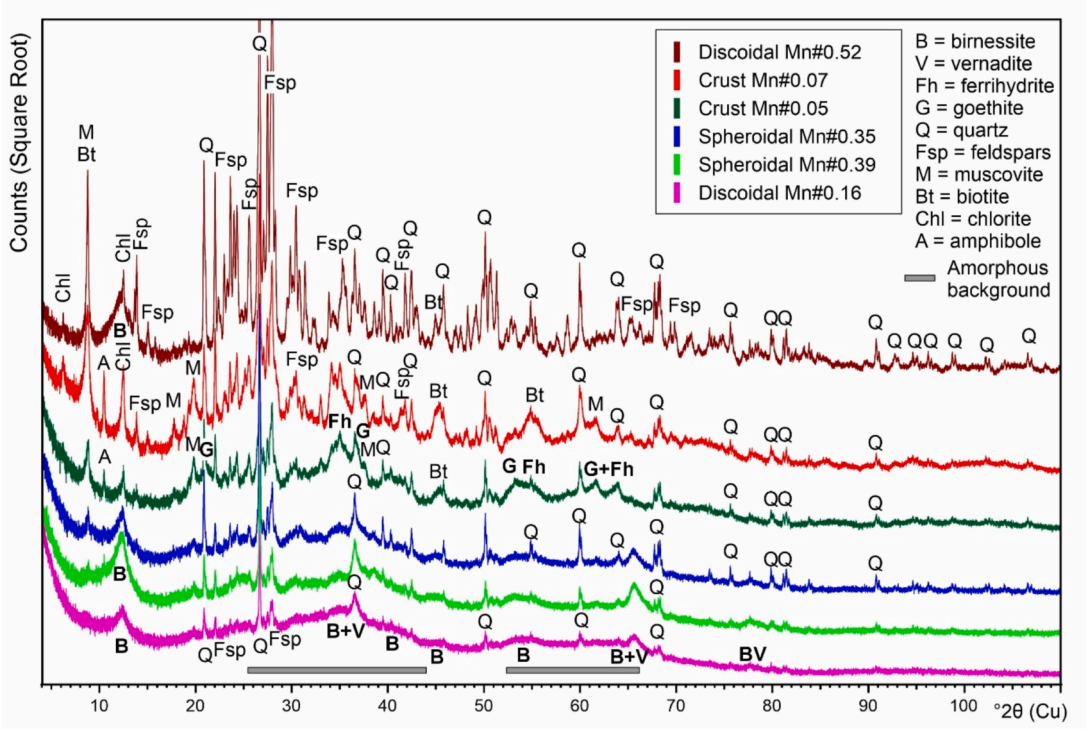

Fig. 4. XRD powder patterns of six bulk samples of Baltic Sea ferromanganese concretions of differing morphotypes, arranged by upward increasing detrital mineral phase content. The samples are named by morphotype and Mn# [atomic Mn/(Mn + Fe)].

by the highest Ti/Zr ratios and total Al contents in this morphotype (Fig. 9a). To evaluate the effects of reworking, we further investigated the CIA/WIP ratio, which represents the combined effects of weathering and quartz dilution (Garzanti et al., 2013), and compared it to the Chemical Index of Quartz-enrichments (CIQ = (172.4–1.7 × CIA − WIP)/WIP) which accurately captures SiO_2 enrichment (Guo et al., 2024). The CIA/WIP vs. CIQ diagram therefore can be used to untangle effects of weathering intensity, mineralogical sorting, and sedimentary recycling (Guo et al., 2024). Based on the biplot (Fig. 9b), the detrital fraction in none of the morphotypes has experienced significant weathering while it has undergone reworking with an increasing order from crust to spheroidal to discoidal.

Water depth does not appear to correlate well with the CIA/WIP ratio or CIQ in crust concretions but shows a significant negative correlation in discoidal and spheroidal concretions (Fig. 9c). This suggests that increasing water depth leads to increased quartz dilution and reworking of the detrital fraction in these two morphotypes.

3.4. Spatial variability

When comparing the elemental contents of ferromanganese concretions from the Baltic Sea to those in the global ocean (Fig. 10), some differences emerge in relation to oceanic and other shelfal precipitates. Overall, the chemical composition of Baltic Sea concretions resembles other shelfal precipitates. The main differences lie in the contents of As, Mo, Pb, S, Sb, and V, which are lower, at less than half the mean contents found in other shelfal regions. Conversely, Rb and W contents are more than double the mean contents observed in other shelfal concretions.

On the other hand, the contents of certain elements (Al, As, Ba, Ca, Fe, Li, Mg, Na, S, Sr, U, and W) in the Baltic Sea concretions are in the same range with those found in oceanic precipitates. Phosphorus (P), Cr, and Rb are notably higher, while other measured elements fall below those commonly observed in the oceanic setting. The element associations to main phases (Fe-rich, Mn-rich and detrital) observed in the Baltic Sea concretions are largely consistent with those reported previously for oceanic precipitates (e.g. Hein et al., 2017; Ren et al., 2024a).

Within the Baltic Sea, geographic location has some impact on the overall chemical composition of the concretions, despite larger variations in the distribution of Fe and Mn phases, detrital component characteristics, and Ce anomaly values across different sampled areas (Fig. 11). In the Gulf of Finland, sampling of all endmember morphotypes revealed that the primary distinctions across these morphotypes are defined by the Ti/Zr ratio and Al content (Fig. 11a and b). Conversely, the Fe/Mn ratio and Ce anomaly values were found to be consistent across all morphotypes within this sampling area (Fig. 11c and d).

Additionally, crust and discoidal concretions were collected from various locations, including the Gulfs of Bothnia and Finland, as well as the Archipelago Sea. For crust concretions, the Al content remained consistent across all sampling sites (Fig. 11b), while the Ti/Zr ratio exhibited a slight increase from the Gulf of Finland to the Gulf of Bothnia (Fig. 11a). Similarly, the Fe/Mn ratio and Ce anomaly values showed a gradual increase in the same order (Fig. 11c and d). The slightly differing Fe/Mn ratio, Ce anomaly values as well as the Ti/Zr ratio might be influenced by the higher occurrence of spring floods in the Gulf of Bothnia (Ostrobothnia region) in comparison to Gulf of Finland, as well as the overall better oxygenated bottom water conditions in the Gulf of Bothnia (Kuosa et al., 2017).

Discoidal concretions exhibited the highest Fe/Mn ratios and Ce anomaly values in the Archipelago Sea, followed by the Gulf of Finland (Fig. 11c and d). The Al content was higher in the Archipelago Sea in comparison to the Gulf of Finland, while the Ti/Zr ratio for the discoidal morphotype was lower in the Gulf of Finland (Fig. 11a and b).

3.5. Stable Pb isotopes

To analyze recent trends and variations in the sources of terrigenous component of the ferromanganese concretions, the outermost 1 mm of concretion samples from three distinct locations in the Baltic Sea was

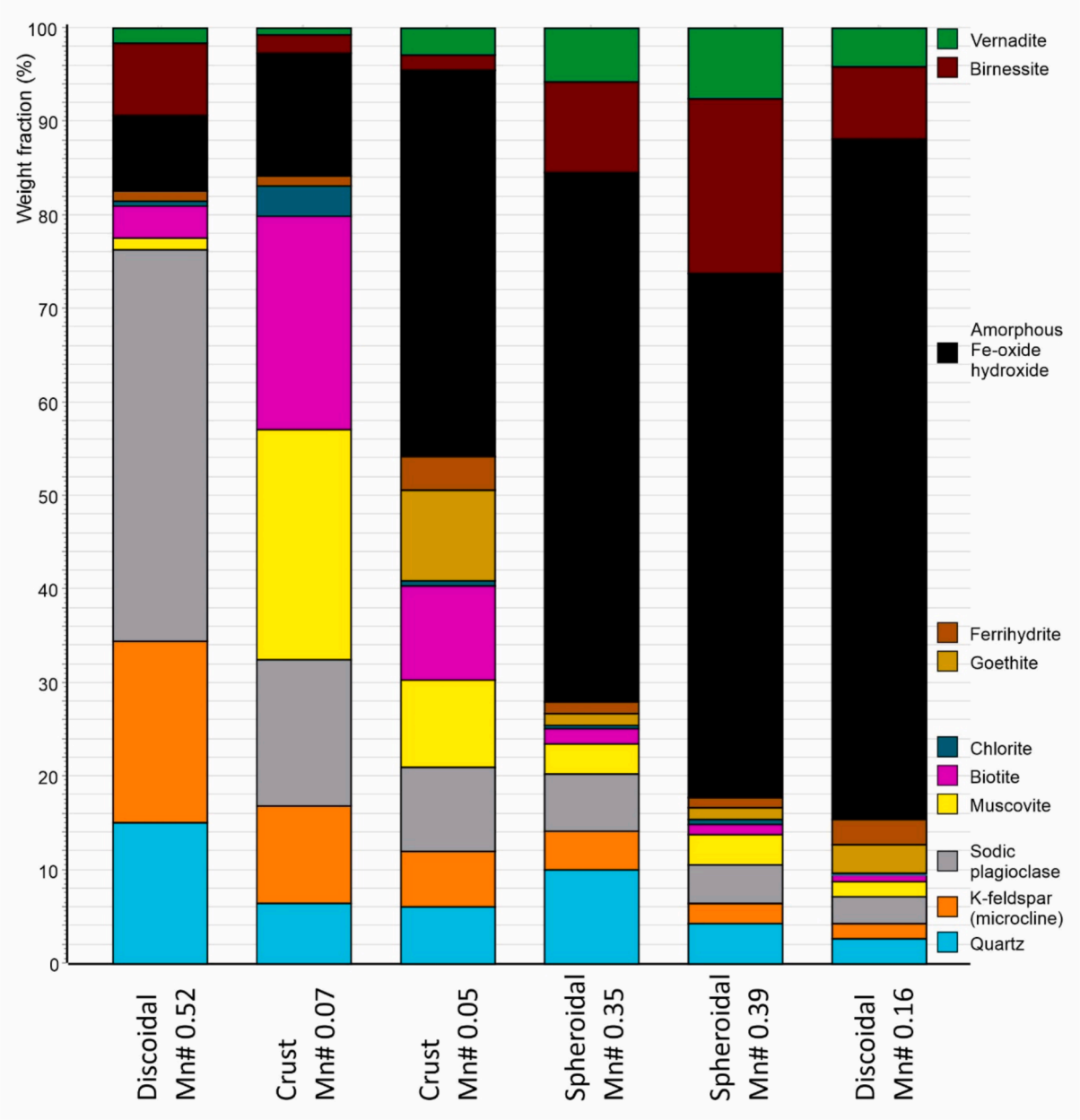

Fig. 5. XRD Rietveld phase composition of six bulk samples of Baltic Sea ferromanganese concretions of different morphotypes in the same order as in Fig. 4.

examined *in-situ* for stable Pb isotope compositions. These locations include the Western Baltic Sea (Mecklenburg Bight), the Eastern Baltic Sea (Gulf of Finland), and the Northern Baltic Sea (Gulf of Bothnia). The obtained Pb isotopic ratios of the samples are presented in Table 3 and in (Wasiljeff et al., 2024b).

In the studied samples, the crust concretion from the Gulf of Finland shows the most radiogenic mean $^{206,207,208}Pb/^{204}Pb$ ratios of ~23.31, ~16.46 and ~41.36, respectively (median: ~23.38, ~16.46, ~41.41; range: ~22.06–24.03, ~16.03–16.81, ~40.21–43.06), followed by the crust from the Gulf of Bothnia ($^{206,207,208}Pb/^{204}Pb$ mean: ~21.99, ~15.44, ~39.09; median: ~21.77, ~15.45, ~38.88; range: ~20.11–25.54, ~14.07–16.35, ~35.35–46.95). The Pb isotope values then decline to the least radiogenic in the discoid from the Mecklenburg Bight ($^{206,207,208}Pb/^{204}Pb$ mean: ~18.85, ~15.70, ~38.67; median: ~18.92, ~15.75, ~38.58; range: ~18.16–20.24, ~15.00–16.27, ~37.63–39.64).

4. Discussion

4.1. Morphological and mineralogical characteristics: associations to bulk element geochemistry

The microscale elemental and mineralogical examination of ferromanganese concretions from the Baltic Sea shows that the discoidal and spheroidal morphotypes are dominated by the alternating growth layers of Fe- and Mn-rich phases, while ferromanganese crust samples are predominantly composed of Fe-rich phases (Fig. 2). The Mn-rich layers primarily consist of phyllomanganates, mainly birnessite (Figs. 3 and 5). These layers form columnar and dendritic growth patterns (Wasiljeff et al., 2024a), aligning with microbially mediated precipitation processes (Blöthe et al., 2015; Heim et al., 2017; Scopelliti and Russo, 2021; Sjöberg et al., 2021) and accelerated growth rates in relatively stagnant hydrodynamic conditions (Josso et al., 2020b; Ren et al., 2023). Although microbial involvement in concretion formation is well-documented (Yli-Hemminki et al., 2014; Sujith and Gonsalves, 2021;

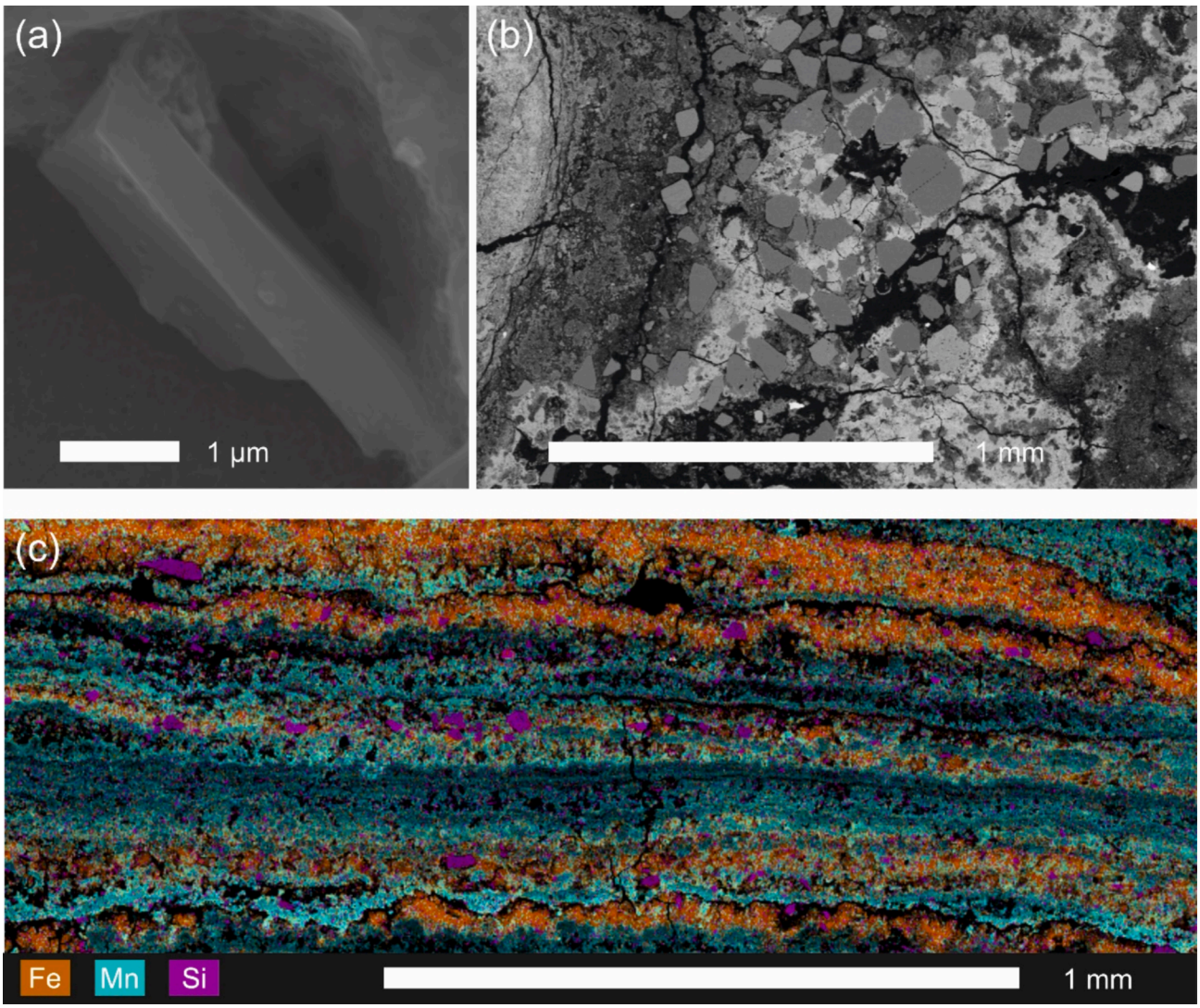

Fig. 6. FE-SEM BSE images of (a) euhedral feldspar grain with few etch pits, (b) Fe-Mn matrix embedded Al-Si containing sub-angular detrital grains, and (c) element map of Fe, Mn and Si showing alternating Fe- and Mn-rich layers with the Fe layers and Fe-Mn interfaces enriched with detrital Si-containing minerals.

Jiang et al., 2022; Shulga et al., 2022; Majamäki et al., 2025), the columnar directional and dendritic branching growth, along with the birnessite mineralogy, can arise not only from biomineralization but also from indirect or direct microbial regulation. Abiotic, random, and surface-normal growth processes can also explain the observed growth patterns and composition (Sutherland et al., 2020). Nonetheless, it is widely accepted that natural Mn oxides are largely biogenic in origin, and biogenic birnessite is often the most common form of these oxides (Tebo et al., 2004; Webb, 2005; Mayanna et al., 2015; Sjöberg et al., 2021). The processes of metal sorption, ion exchange, and coprecipitation by birnessite and other Mn oxides are influenced by various factors, including crystallinity, surface area of the oxide particles, Eh, pH, and the amount of competing ligands (e.g. Post, 1999; Tebo et al., 2004). Generally, sorption capacity of birnessite is significantly higher for many metal cations than that of Fe hydroxides (Li et al., 2020). This is reflected in the positive correlation of Ba, Cd, Cu, Mo, Ni, Sb, and Sr (as well as the nonmetallic S) with Mn and negative correlation with Fe in our data (Fig. 8), underscoring the tendency of Mn oxides to readily sorb these elements in their structure and surface (Tessier et al., 1996; Luo et al., 2017; Qiao et al., 2020; Karimian et al., 2021; Hayles et al., 2021; Tani et al., 2021; Ren et al., 2022, 2024a).

The Fe-rich mineral phase in the concretions is composed of poorly crystalline ferrihydrite (Figs. 3 and 5), which together with the predominantly high Fe/Mn ratios observed in the samples, could indicate abiotic hydrogenetic precipitation, involving surface and inorganic colloidal reactions with oxic bottom seawater and/or porewater (Usui et al., 1989; Koschinsky and Halbach, 1995; Heller et al., 2018). In hydrogenetic oceanic ferromanganese concretions and polymetallic nodules, Pb and high field strength (HFS) elements have been commonly reported to be associated with the poorly-crystalline Fe oxide phases (Koschinsky and Hein, 2003; Bau and Koschinsky, 2009; Schmidt et al., 2014; Josso et al., 2017; Guan et al., 2019; Ren et al., 2024a), reflecting hydrolytic release of terrigenous materials (Guan et al., 2019) and concomitant formation of poorly-crystalline Fe oxide phases. High positive correlations of Pb and REE + Y with Fe, but low positive correlations with Al, and negative correlations with Mn (Fig. 8) suggest a similar association of these elements to predominantly Fe phases in the Baltic Sea concretions. Additionally, the poorly crystalline Fe-rich phase readily scavenges anionic species of As, P and V from the surrounding waters (Glasby, 2006), and this is highlighted by the association of these elements to Fe also in our data. The relatively high Fe contents (and high Fe/Mn ratios) observed here are a characteristic feature of concretions found in continental shelf environments and have been explained to reflect increased terrigenous influence and changes in hydrodynamic conditions, where higher energy events and the consequent reworking of underlying sediments leads to the increased Fe precipitation (e.g.

Table 2
Elemental composition of the Baltic Sea ferromanganese concretion types.

	Crust (n = 19)				Discoidal (n = 15)				Spheroidal (n = 14)			
	Mean	Median	Min	Max	Mean	Median	Min	Max	Mean	Median	Min	Max
Fe (wt%)	18.7	19.5	6.84	29.9	18.0	13.7	3.17	35.1	16.4	16.4	6.53	24.0
Mn	4.99	3.04	0.36	16.8	7.36	6.37	1.44	13.2	8.48	8.11	4.88	14.0
Fe/Mn	13.9	5.1	0.41	65.2	6.94	4.11	0.56	28.7	2.36	1.98	0.48	4.69
Mn#	0.21	0.16	0.02	0.71	0.30	0.20	0.03	0.64	0.36	0.34	0.18	0.67
Al	4.29	4.55	1.61	7.07	2.18	2.01	1.12	4.94	2.07	2.08	1.48	2.66
Ba	0.15	0.11	0.06	0.45	0.23	0.23	0.08	0.36	0.25	0.24	0.19	0.42
Ca	1.11	1.15	0.63	1.35	1.16	1.16	0.96	1.28	1.28	1.32	1.02	1.49
Mg	1.30	1.24	0.93	2.06	0.87	0.95	0.30	1.19	0.89	0.90	0.74	1.18
Na	1.05	1.02	0.73	1.56	1.02	0.96	0.58	2.83	0.95	0.95	0.76	1.17
K	1.92	2.00	1.06	3.04	1.34	1.33	0.57	3.04	1.20	1.19	0.91	1.83
Ti	0.24	0.23	0.05	0.47	0.08	0.05	0.03	0.22	0.06	0.06	0.03	0.08
P	1.03	0.94	0.22	2.21	1.11	0.91	0.16	1.98	1.24	1.32	0.43	1.85
S	0.06	0.05	0.02	0.12	0.07	0.08	0.03	0.11	0.08	0.07	0.04	0.12
As (ppm)	116	100	25	240	54	50	16	195	49	48	8	89
Be	2.3	2.3	0.8	3.3	1.9	1.9	1.0	2.9	1.4	1.4	0.9	1.7
Bi	0.2	0.1	<0.01	0.4	0.1	0.1	<0.01	0.4	0.1	0.1	<0.01	0.1
Cd	2.7	1.6	0.3	7.7	3.0	2.6	0.6	4.9	4.2	4.2	2.0	6.9
Co	83	79	24	185	111	94	43	277	93	98	55	122
Cr	54	52	<2	104	63	14	2.2	709	11	13	<2	17
Cu	38	33	20	72	29	30	14	45	34	32	20	57
Hf	2.3	2.4	0.9	4.2	1.5	1.2	0.6	4.0	1.6	1.7	0.9	2.4
Mo	24	16	2.2	134	31	27	3.3	108	12	9.5	5.0	27
Nb	8.8	9.2	0.7	18	2.3	0.8	0.5	7.9	1.0	1.0	0.3	2.1
Ni	146	92	48	336	178	167	64	378	144	149	68	206
Pb	20	18	2.4	43	23	17	5.1	64	18	13	2.6	41
Rb	101	105	36	201	55	42	22	112	44	40	29	87
Sb	2.0	1.4	0.8	7.6	1.3	1.3	0.5	2.4	1.8	2.1	0.6	2.8
Sc	9.2	10	2.7	19	3.8	3.2	1.8	7.9	3.8	3.8	2.8	4.7
Sn	1.9	2.0	<0.5	3.6	0.8	0.6	<0.5	2.1	0.3	0.3	<0.5	0.4
Sr	430	423	181	1280	679	709	303	1040	830	821	706	999
Th	9.7	9.6	3.0	21	4.6	3.3	3.0	12	4.9	4.8	2.7	7.0
U	9.9	10	5.5	14	12	12	3.5	17	9.8	9.3	6.4	15
V	112	112	29	168	58	41	17	156	34	35	18	47
W	3.1	1.5	<0.2	15	151	2.5	<0.2	1770	1.0	0.5	<0.2	3.1
Y	32	32	17	52	35	34	11	58	30	31	22	36
Zn	243	208	105	624	229	200	91	405	347	266	133	669
Zr	87	86	39	152	66	54	30	152	69	72	38	106
ΣREE	214	213	87	314	205	212	90	381	193	207	111	271

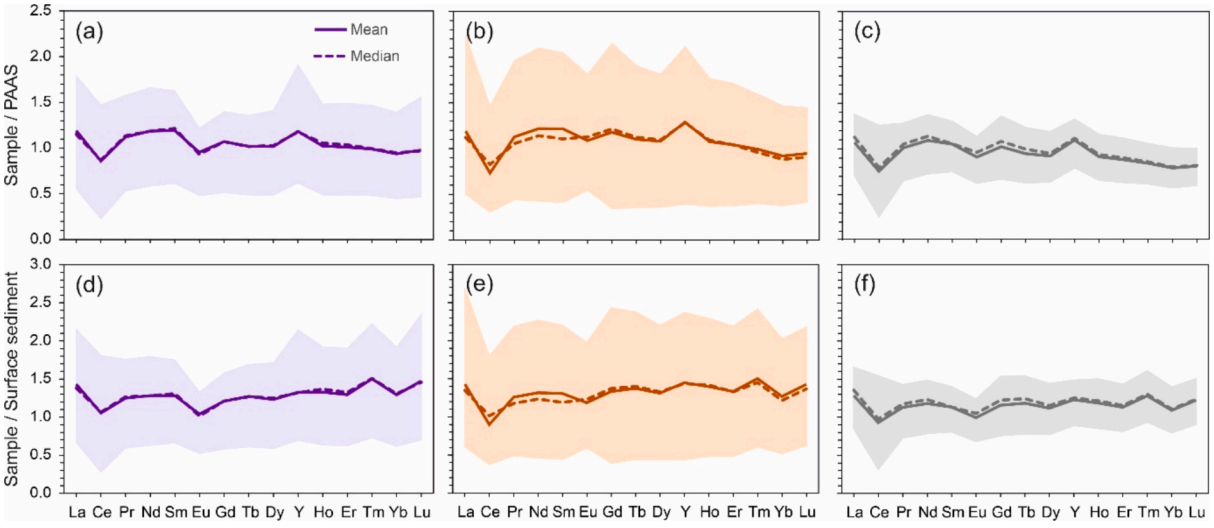

Fig. 7. PAAS (Pourmand et al., 2012) normalized REY patterns in (a) crust, (b) discoidal, and (c) spheroidal Baltic Sea ferromanganese concretions. REY normalized to Baltic Sea surface sediment composition for the corresponding morphotypes (d–f). Bold line represents mean values, dashed line median and the shaded area range.

Winterhalter, 2004; Vereshchagin et al., 2019 and references therein; Shulga et al., 2022). However, notably thick (several hundreds of microns) Fe-rich growth zones observed in the shallow water concretions render purely hydrogenetic precipitation improbable (Vereshchagin et al., 2019), as this process is conventionally understood to occur at a very slow rate (Cowen et al., 1993; Koschinsky and Hein, 2003). In the Baltic Sea, the growth rates are considered to be exceptionally high even in the realm of continental shelf Fe-Mn precipitates, comparable with

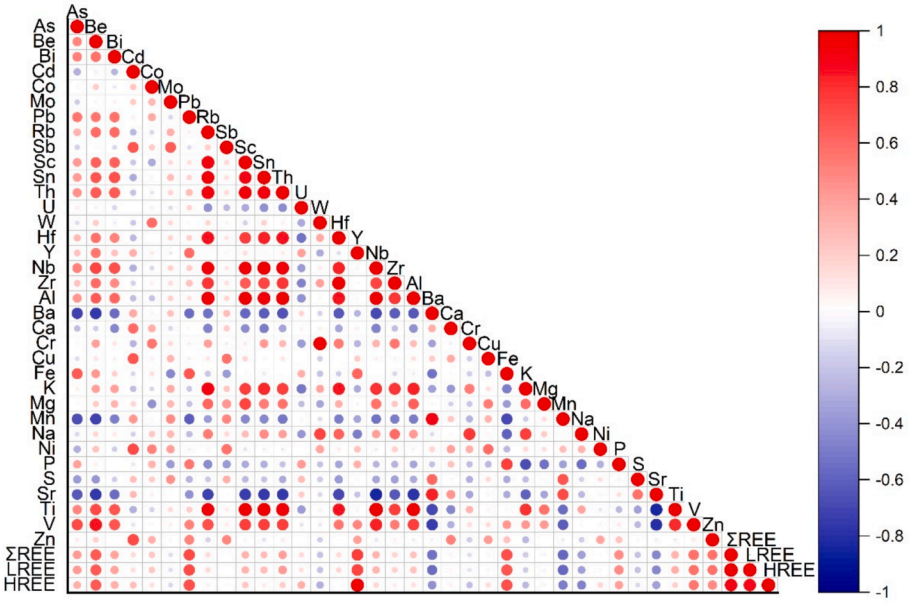

Fig. 8. Pearson correlation coefficient plot for the analyzed element concentrations of Baltic Sea ferromanganese concretion samples.

those found in freshwater lake concretions (Krishnaswami and Moore, 1973; Moore et al., 1980; Asikainen and Werle, 2007). The trace element composition of Baltic Sea ferromanganese concretions also aligns with previously published data on lake and other shelfal concretions and can be distinguished from oceanic hydrogenetic and diagenetic crusts and polymetallic nodules using a ternary diagram of Co-Cu-Zn (Fig. 12). The overall contents of the three elements are lower in shelfal and freshwater precipitates (cf. Baturin, 2019), which is due to their higher growth rates, reducing the time available for metal accumulation. Cobalt (Co) is the dominant trace element in hydrogenetic oceanic precipitates and Cu is dominant in diagenetic oceanic nodules. In contrast, the higher proportion of Zn in shelfal and freshwater concretions, as compared to the deep sea concretions, seems to associate with the higher Zn concentrations in the waters of coastal sea areas, estuaries, and freshwater systems compared to the deep ocean (Neff, 2002; de Souza Machado et al., 2016). This increase is attributed to greater terrestrial influx, higher biological productivity, and anthropogenic inputs (Moore et al., 1980; Hlawatsch et al., 2002; Verstijnen et al., 2024). The proportionally high contents of As and P in the Baltic Sea concretions and their association to ferrihydrite (Fe-rich phase) further highlights the genetic similarity to lacustrine concretions, which are considered to precipitate in varying proportions through diagenetic (porewater) and hydrogenetic (water column) processes (Couture et al., 2018; Hayles et al., 2021). Employing the ternary Fe-Mn-(Ni + Cu)*10 diagram proposed by Halbach et al. (1981), the data scatter is consistent with the high Fe and lower Ni and Cu contents relative to oceanic precipitates (Fig. 13a). This is evident as the data plots closely parallel to the Fe/Mn axis within the hydrogenetic field. However, the data appears to be plotted along a mixing line between the hydrogenetic and diagenetic fields, likely reflecting the differing hydrodynamic and redox conditions in the near-bottom environment where the concretions form that affects the Fe/Mn ratio.

The Ce/Ce* ratio is another common metric to differentiate ferromanganese precipitates of hydrogenetic and diagenetic origins in the oceanic setting (Hein et al., 2020). Upon oxidation, which is limited by the concretion growth rate, Ce becomes immobilized and ceases to react with the surrounding seawater or porewater (Bau et al., 2014; Heller et al., 2018). When coupled to Nd contents, the slightly negative to intermediate Ce anomaly values observed in the Baltic Sea concretions (Fig. 13b), which are close to one, may indicate early diagenetic formation (Bau et al., 2014). Diagenetic precipitation commonly occurs from porewaters due to sudden changes in redox conditions within suboxic sediments or at the sediment–water interface, leading to the oxidation of Mn(II)-rich porewater and subsequent precipitation of 7 Å and 10 Å phyllomanganates (Glasby, 2006; Hein and Koschinsky, 2014; Wegorzewski and Kuhn, 2014; Koschinsky and Hein, 2017). The distinct clusters of data from crusts and discoids, as opposed to the data from spheroidal concretions in the diagram (Fig. 13b), likely reflect different formation processes and diagenetic conditions (Zhang et al., 2025). These processes are influenced by various factors, including variations in benthic efflux and groundwater seepage (Johannesson et al., 2011; Abbott et al., 2016), as indicated by the Nd contents. In our data, increasing Fe/Mn ratios are also positively correlated with higher Ce/Ce* values and an increase in the total contents of REEs and other Fe-associated elements. These relationships are observed for all morphotypes but are most prominent in the spheroidal concretions, which may be related either to their relatively fast growth rate or differing growth environment that is reflected in the Fe/Mn ratio and thus the distribution of elements across the binding phases (Takahashi et al., 2007). In contrast to the spheroidal morphotype, this correlation is not equally evident in the crust and discoidal concretions, indicating that some other mechanism(s) unrelated to the Fe/Mn ratios may overprint changes in the apparent growth rate in relation to the Fe phase associated element contents and Ce anomaly values.

4.2. *Terrigenous influence and detrital material*

The results indicate that the crust concretions have the highest abundance of terrigenous detrital material, followed by the discoidal and spheroidal morphotypes, respectively. The elevated levels of Ti and Al in the crust concretions (Figs. 9a and 11b; Table 2) suggest a stronger terrigenous influence, possibly under more dynamic and higher-energy conditions. This is further supported by the magnetic properties, which show higher amounts of detrital magnetic phases in the crust morphotype (Wasiljeff et al., 2024a).

Titanium (Ti) and Zr are known to be resistant to weathering and are predominantly found in recalcitrant silicate minerals like rutile and zircon, respectively (Dypvik and Harris, 2001; Kylander et al., 2013). Previous research suggests that Ti levels may reflect the quantity of detrital sediments transported into coastal or lacustrine systems via rivers and surface runoff (Biskaborn et al., 2012), whereby the elevated Ti/Zr ratio observed in the crust concretions could indicate either an increase in clay and silt fraction or a depletion in coarser particles (Liu

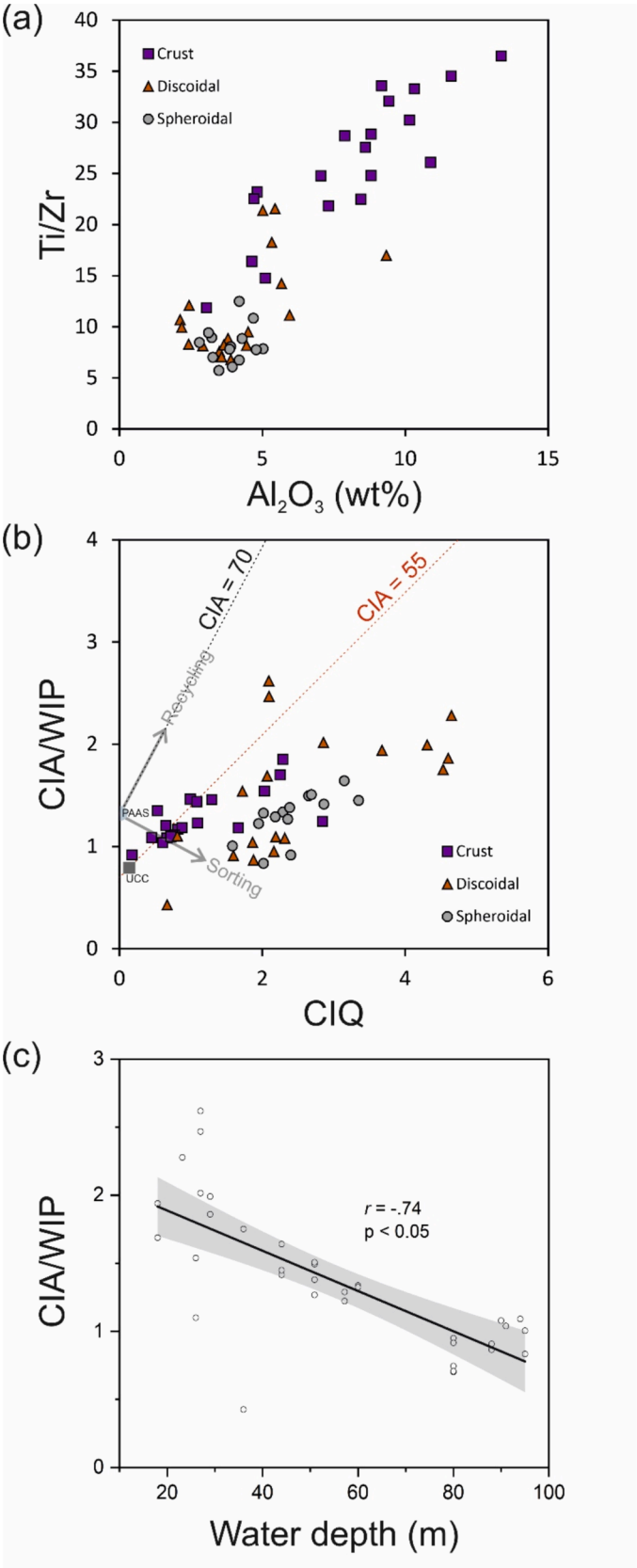

Fig. 9. (a) Ti/Zr ratio versus Al_2O_3 contents in the Baltic Sea ferromanganese concretions of different morphotypes. (b) CIA/WIP versus CIQ diagram for different morphotypes with predicted trends of increasing hydrodynamic sorting and sedimentary recycling. UCC = Upper Continental Crust, PAAS = Post Archean Australian Shale. (c) Water depth versus CIA/WIP ratio of discoidal and spheroidal morphotype samples. Black line is linear fit and the gray shaded area 95 % confidence interval.

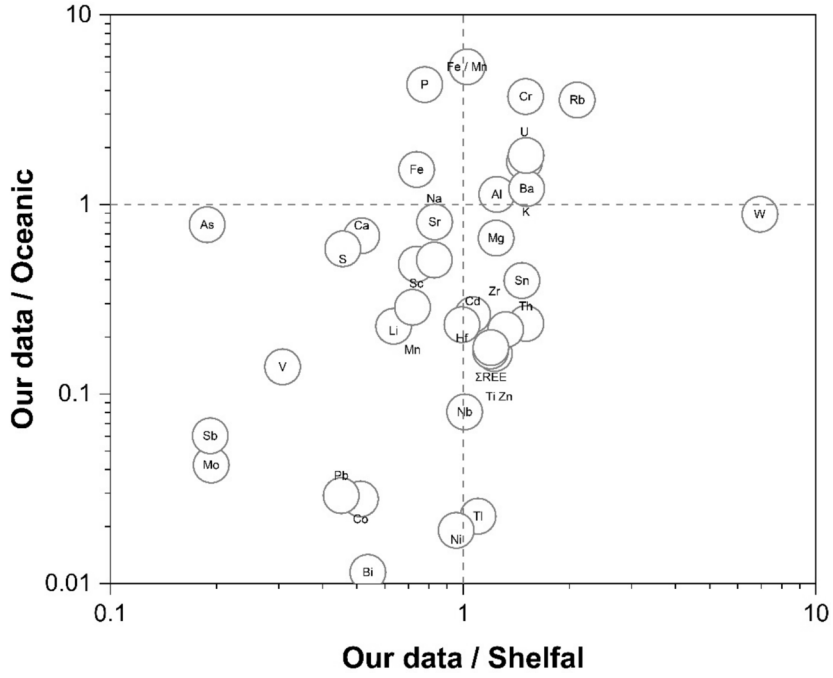

Fig. 10. Comparison of Baltic Sea ferromanganese concretion elemental composition to shelfal (Baturin, 2019) and oceanic (Dekov et al., 2021; Ren et al., 2024a) concretions.

et al., 2022). Furthermore, variations in Ti and Zr concentrations can act as qualitative or semi-quantitative markers for the presence of total detrital material (Francke et al., 2020). Similarly, Al indicates the overall proportion of lithogenic particles and may be less affected by hydrodynamic conditions, making it useful for estimating changes in the energy dynamics of terrestrial material supply (Bertrand et al., 2012). These findings align with XRD results, which show a higher clay fraction in crust concretions (Figs. 4 and 5), suggesting they are formed in environments with a stronger terrigenous flux.

On the other hand, the detrital material in the spheroidal and discoidal concretions appears to be more mature (Figs. 4 and 5) and has undergone significant transport and reworking (Fig. 9b) before incorporation into the concretions. This could imply that the material in these morphotypes originates from more distant sources. Additionally, the significant negative correlation between water depth and the CIA/WIP ratio or CIQ in discoidal and spheroidal concretions (Fig. 9c) suggests that greater depths lead to increased quartz dilution and reworking of the detrital fraction.

These differences in the detrital material and weathering indicators between the morphotypes may reflect varying depositional environments and sedimentary processes in the Baltic Sea, with crust concretions forming closer to shorelines in higher-energy conditions compared to spheroidal and discoidal morphotypes, which are more influenced by reworking and transport from distant sources.

4.3. Pb isotope ratios: indications of ferromanganese material sources

The high Fe/Mn ratios and distribution of Pb in association with the higher Fe contents indicate a major terrigenous Fe component in the Baltic Sea concretions (Winterhalter, 2004; Ling et al., 2005; Baturin and Dubinchuk, 2011; Hein et al., 2017; Guan et al., 2019). Given that the input of Pb (alongside the matrix-forming Fe and Mn) into the shelf environment is primarily controlled by riverine transport and is influenced by scavenging through ferromanganese precipitates, the stable Pb isotope composition of the concretions reflects the origin of catchment-derived, concretion-forming materials (Frank, 2002). The Pb isotopic signatures of the concretions are more radiogenic in the northern and north-eastern sampled locations (the Gulf of Bothnia and the Gulf of Finland) in comparison to south-western Baltic Sea (Mecklenburg Bight). The sample from the Mecklenburg Bight (Blink-2020-1a) has Pb isotopic composition that is close to the Upper Continental Crust values whereas the other samples (MGBC-2021-4-1 and Levy2) are consistent with more radiogenic felsic igneous rock compositions (Doucet et al., 2023). The Gulf of Bothnia sample (Levy2) shows the most internal variation in its Pb isotopic composition and is also the only one that shows a clear trend over time: the younger growth layers tend to have slightly more radiogenic Pb than the older ones. The increase in radiogenic Pb content in the younger parts of the concretion could reflect changes in provenance and increased weathering and erosion of the granitic bedrock of the catchment area. The latter is due to rising precipitation and riverine flow volumes, earlier snowmelt and overall effects of climate change that has impacted the riverine transport patterns in certain parts of the northern coastal areas of the Gulf of Bothnia (Lintunen et al., 2024). In contrast to the Levy2 sample, the samples from the Gulf of Finland (MGBC-2021-4-1) and Mecklenburg Bight (Blink-2020-1a) show subtler changes in the isotopic composition without systematic temporal variation. When plotted in a ternary diagram of ^{206}Pb, ^{207}Pb and ^{208}Pb, the compositions largely follow those of European agricultural soils (Fig. 14), which, in turn, predominantly reflect the isotopic signatures of the underlying bedrock (Reimann et al., 2012, 2014a,b). The isotopic composition of the two samples from the northern and north-eastern parts of the Baltic Sea (MGBC-2021-4-1 and Levy2) are roughly coincident with those of the Precambrian Craton of NE Europe (Fennoscandian Shield), whereas the sample from Mecklenburg Bight (Blink-2020-1a) has values commonly obtained in the region of Paleozoic platform in western Europe. The partial overlap of isotopic values with those of European Pb deposits and Mississippi Valley (Sangster et al., 2000; Tomczyk, 2022) in the ternary plot aligns with a putative pollution Pb component in the concretions, but the observed compositions can be explained with variations in the local source of catchment-derived material.

4.4. Implications for growth and diagenetic evolution of shelfal ferromanganese concretions: a case study from the Baltic Sea

Shelfal ferromanganese concretions form primarily through early

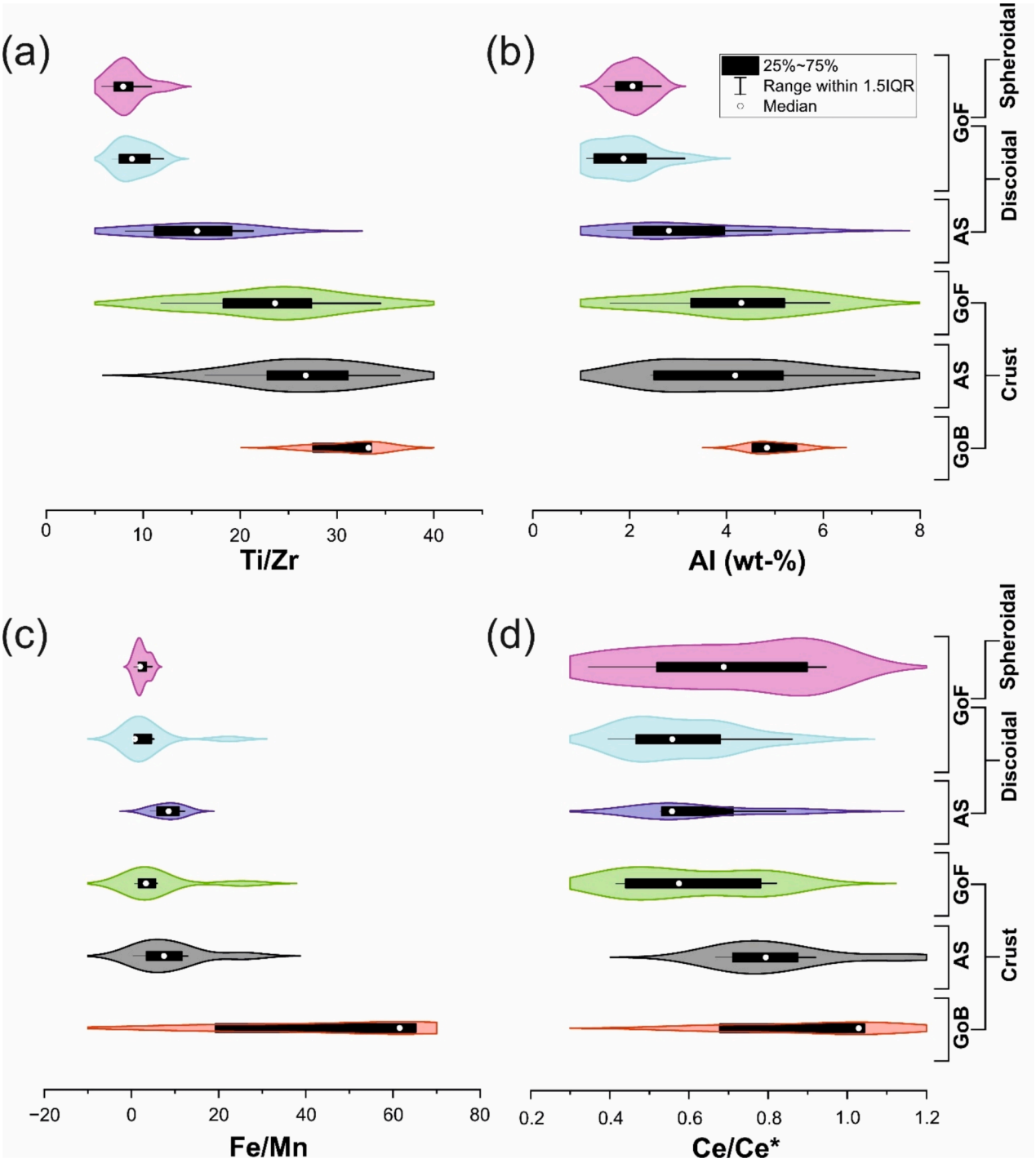

Fig. 11. Geochemical characteristics of ferromanganese concretions versus morphotype and sampling location in the Baltic Sea: (a) Ti/Zr ratio, (b) Al content, (c) Fe/Mn ratio and (d) Ce/Ce* ratio. GoB = Gulf of Bothnia, AS = Archipelago Sea, GoF = Gulf of Finland.

diagenetic processes and their growth is controlled by the interplay of hydrodynamic conditions, terrigenous material input, and redox fluctuations (Zhamoida et al., 1996; Glasby et al., 1997; Baturin, 2010; Vereshchagin et al., 2019; Wasiljeff et al., 2024a; this study). Across various shelf regions, such as the Kara Sea, Black Sea, and Baltic Sea, these factors contribute to the development of distinct concretion morphotypes (in the Baltic Sea recognized as crust, discoidal, and spheroidal), each linked to specific environmental conditions. While these broad processes are common across shelf seas, the Baltic Sea provides a case study highlighting key interactions that drive the formation and diagenetic evolution of shelfal ferromanganese concretions.

Higher-energy and/or shallower environments are characterized by the formation of Fe-rich concretions, mainly the crust morphotype. In these settings, near-bottom flows facilitate the mixing of terrigenous detrital material into the growing ferromanganese matrix (Fig. 15). Previous studies have documented that ferromanganese concretions on the Baltic Sea floor, as well as other shelf sea areas, may occasionally be covered by a transient layer of very organic-rich fluffy mud (Fig. 15; Hlawatsch et al., 2002; Winterhalter, 2004; Zhamoida et al., 2017; Shulga et al., 2022; Wasiljeff et al., 2024a). Intermittent coverage by the organic-rich fluffy mud can create mildly reducing conditions, where the mobility of Fe and Mn are controlled by seasonally fluctuating oxygen

Table 3
Descriptive statistics of Pb isotope ratios in three ferromanganese concretions from the Baltic Sea.

Sample	Location	n		Mean	Median	SD	Min	Max
Blink-2020-1a	MB	39	$^{206}Pb/^{204}Pb$	18.852	18.917	0.351	18.155	20.237
			$^{207}Pb/^{204}Pb$	15.704	15.745	0.308	14.999	16.267
			$^{208}Pb/^{204}Pb$	38.666	38.583	0.488	37.629	39.638
MGBC-2021-4-1-B	GoF	40	$^{206}Pb/^{204}Pb$	23.312	23.384	0.445	22.055	24.031
			$^{207}Pb/^{204}Pb$	16.456	16.464	0.191	16.033	16.808
			$^{208}Pb/^{204}Pb$	41.364	41.408	0.648	40.211	43.063
Levy2	GoB	40	$^{206}Pb/^{204}Pb$	21.989	21.769	1.264	20.109	25.538
			$^{207}Pb/^{204}Pb$	15.440	15.450	0.443	14.073	16.345
			$^{208}Pb/^{204}Pb$	39.085	38.884	1.779	35.346	46.954

MB = Mecklenburg Bight, GoF = Gulf of Finland, GoB = Gulf of Bothnia.

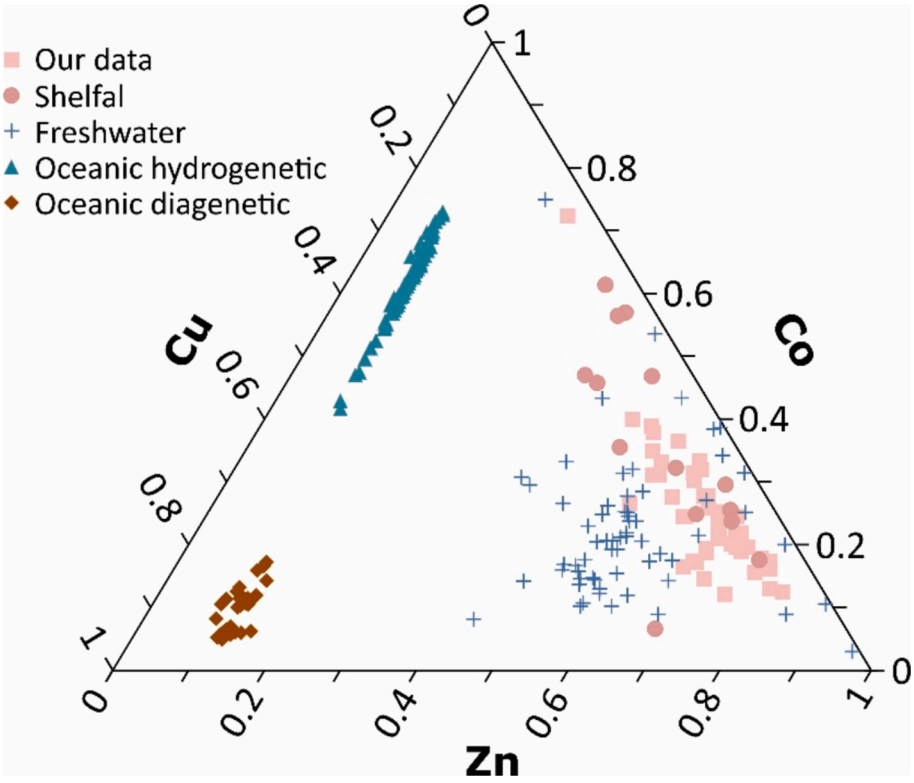

Fig. 12. Ternary diagram of Cu, Co, and Zn contents of Baltic Sea concretions (our data), other shelfal concretions (Baturin and Dubinchuk, 2009; Zhamoida et al., 2017; Baturin, 2019), freshwater concretions (Moore et al., 1980; Williams and Owen, 1992; Baturin, 2019; Hayles et al., 2021) as well as oceanic hydrogenetic (Hein et al., 2015; Ren et al., 2024a) and diagenetic (Dekov et al., 2021) concretions.

distribution in the fluffy layer (Hlawatsch et al., 2002), leading to the partial dissolution and etching of concretions (Fig. 15a). Mn phases are preferentially dissolved under these conditions (Davison, 1993; Manceau et al., 2014), while Fe-rich phases precipitate (or are retained) (Müller et al., 1988; Stumm and Morgan, 1996), forming thick, hydrogenetic-like layers (Fig. 15b). The removal of the fluffy layer by near-bottom currents can promote Mn transfer to the water column and enhance the formation of Fe-rich phases (Fig. 15b; Shulga et al., 2022). Furthermore, the fluffy mud transports detrital minerals (Löffler et al., 2000) that are incorporated, and based on our findings, diagenetically redistributed in the concretions (Fig. 15a and b) due to the preferential dissolution of Mn phases. This process is highlighted by SEM observations, showing accumulations of terrigenous material at the interfaces of Fe-Mn-rich zones, and altered or etched detrital mineral grains (Fig. 6a–c), and is also consistent with the propensity of Fe oxyhydroxides to nucleate around detritus unlike Mn oxides (Hein et al., 2017). Therefore, the admixing of accessory detrital minerals further contributes to the characteristic Fe-enrichment observed in these concretions.

In contrast, concretions in lower-energy environments (Fig. 15c), are dominated by Mn-rich morphotypes, mainly spheroidal and occasionally discoidal (Fig. 15d). These concretions develop primarily under the influence of suboxic to anoxic conditions, where Mn is diagenetically remobilized from sediments and incorporated into the concretions through microbial processes (Fig. 15d; Wasiljeff et al., 2024a), with the associated trace element intake influenced by sediment porewaters (Dekov et al., 2021) and remineralization of bioparticles (Verlaan and Cronan, 2022; Ren et al., 2024a,b) in the fluffy layer. In these lower-energy environments, contrasting the higher-energy regime, the intermittent fluffy mud cover may act as a barrier that prevents Mn from diffusing into the seawater (Fig. 15c; Shulga et al., 2022), likely promoting *in-situ* microbial and biomineralization processes (Wasiljeff

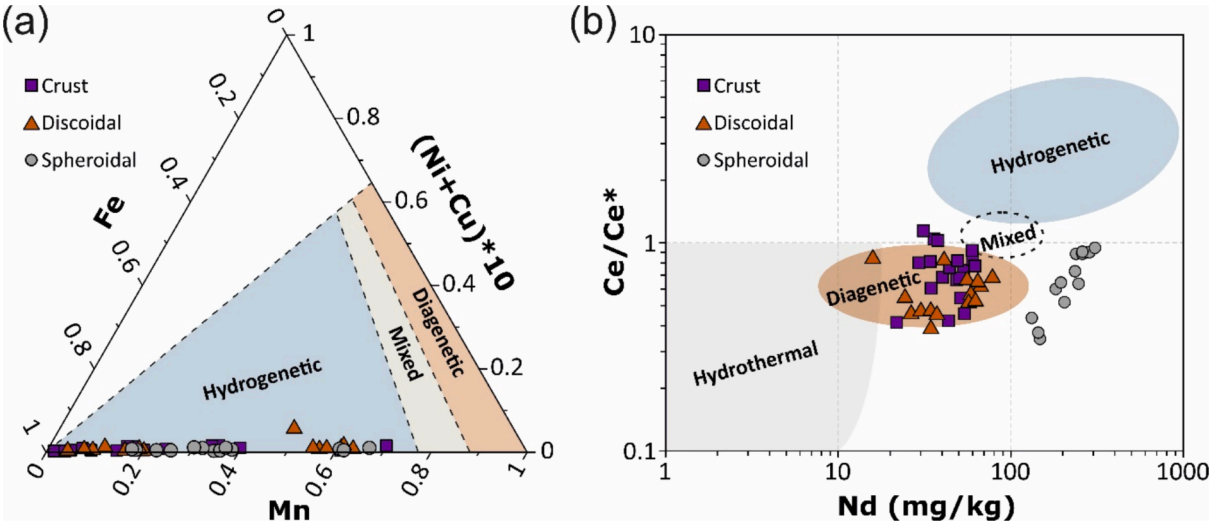

Fig. 13. Discrimination diagrams of seafloor ferromanganese concretions. (a) ternary diagram of Fe-Mn-(Cu + Ni)*10 (Halbach et al., 1981; Wegorzewski and Kuhn, 2014) and (b) Ce/Ce* ratio versus Nd content plot of Bau et al. (2014).

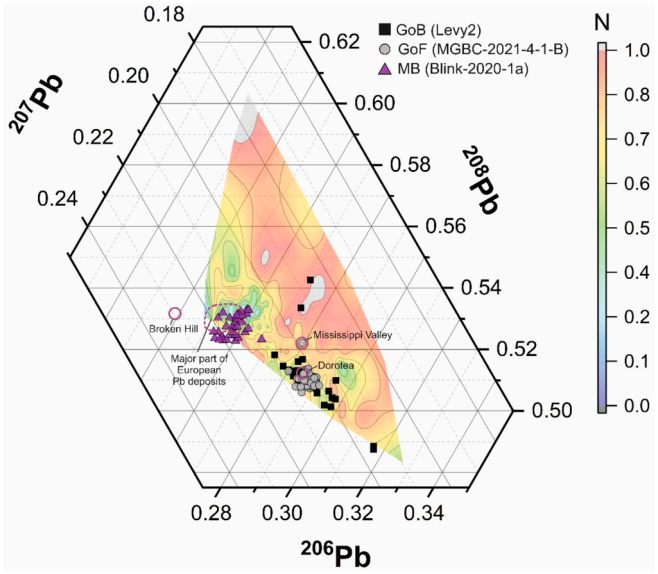

Fig. 14. Ternary plot of the relative proportions of ^{206}Pb, ^{207}Pb and ^{208}Pb of three ferromanganese concretion samples from different parts of the Baltic Sea. The heat map ranging from 0 (south) to 1 (north) depicts European agricultural soil isotopic signatures (Reimann et al., 2012, 2014a,b). Additionally, some European Pb deposits and Broken Hill and Missisippi Valley type ores (Sangster et al., 2000) are included in the figure.

et al., 2024a). This results in relatively continuous concretion growth, often characterized by poorly crystalline birnessite-like mineralogy with porous, columnar and branched dendritic growth patterns (Sjöberg et al., 2018, 2021).

In shelf seas with relatively large catchment areas, such as the Baltic Sea, input from rivers contributes additional trace elements and detrital minerals to concretions. The fluffy mud layer frequently covering the seafloor in these areas not only serves as a barrier that controls Mn cycling but also transports the terrestrial material that becomes incorporated into the concretions and influences their trace element composition spatially. Most of the organic matter in the fluffy mud originates from seasonal primary production in the surface waters, later transported along the seafloor as thin, transient layers (Ksenia et al., 2001; Leipe et al., 2011). This fluffy layer exhibits both seasonal and spatial variations in trace element composition (Pempkowiak et al., 2005), which is reflected also in the geographically differing concretion bulk geochemistry and stable Pb isotope compositions (Figs. 11 and 14), highlighting the importance of terrestrial input from catchment sources as well as local near-bottom conditions. These findings suggest that the combined effects of hydrodynamics, redox fluctuations, and terrigenous input from catchment sources govern both the rate of shelfal concretion growth and the geochemical signatures preserved within them.

5. Conclusions

Ferromanganese concretions from the Baltic Sea provide important insights into the formation mechanisms and diagenetic evolution of shelfal ferromanganese concretions. The Baltic Sea concretions are primarily composed of Fe and Mn mineral phases, with Fe-rich growth zones dominated by 2-line ferrihydrite, while Mn-rich layers are predominantly composed of birnessite, likely of biogenic origin. The Nd contents and slightly negative to intermediate Ce anomaly values observed in the concretions suggest early diagenetic formation conditions. An important factor controlling the concretion morphology and composition may be the intermittent occurrence of a very organic-rich fluffy mud cover layer, which is controlled by the near-bottom flows, transports detrital minerals, and impacts the redox conditions and potentially microbial activity in the concretions. The preferential reductive dissolution of Mn-phases results in the diagenetic redistribution of detrital minerals on the interfaces to Fe-phase dominated zones, as well as the precipitation of thick Fe-rich growth layers.

Crust concretions exhibit high concentrations of Al and Ti, along with an elevated Zr/Ti ratio, reflecting the incorporation of a greater proportion of terrigenous detrital minerals and the concretion formation under high-energy conditions, typically in shallow waters. In contrast, the detrital fraction of spheroidal concretions is characterized by high CIQ values and the lowest Zr/Ti ratio, indicating a higher degree of sediment recycling and hydrodynamic sorting and the concretion formation in low-energy environments, typically in deeper waters. Finally, discoidal concretions show intermediate values, suggesting they form in varied environmental conditions.

Furthermore, the geographic distribution of ferromanganese concretions within the Baltic Sea shows that regional environmental conditions, including proximity to terrestrial inputs and flow regime, influence their bulk geochemistry and stable Pb isotope composition.

The morphology and composition of ferromanganese concretions in shelf sea regions, including the Baltic Sea, are primarily governed by

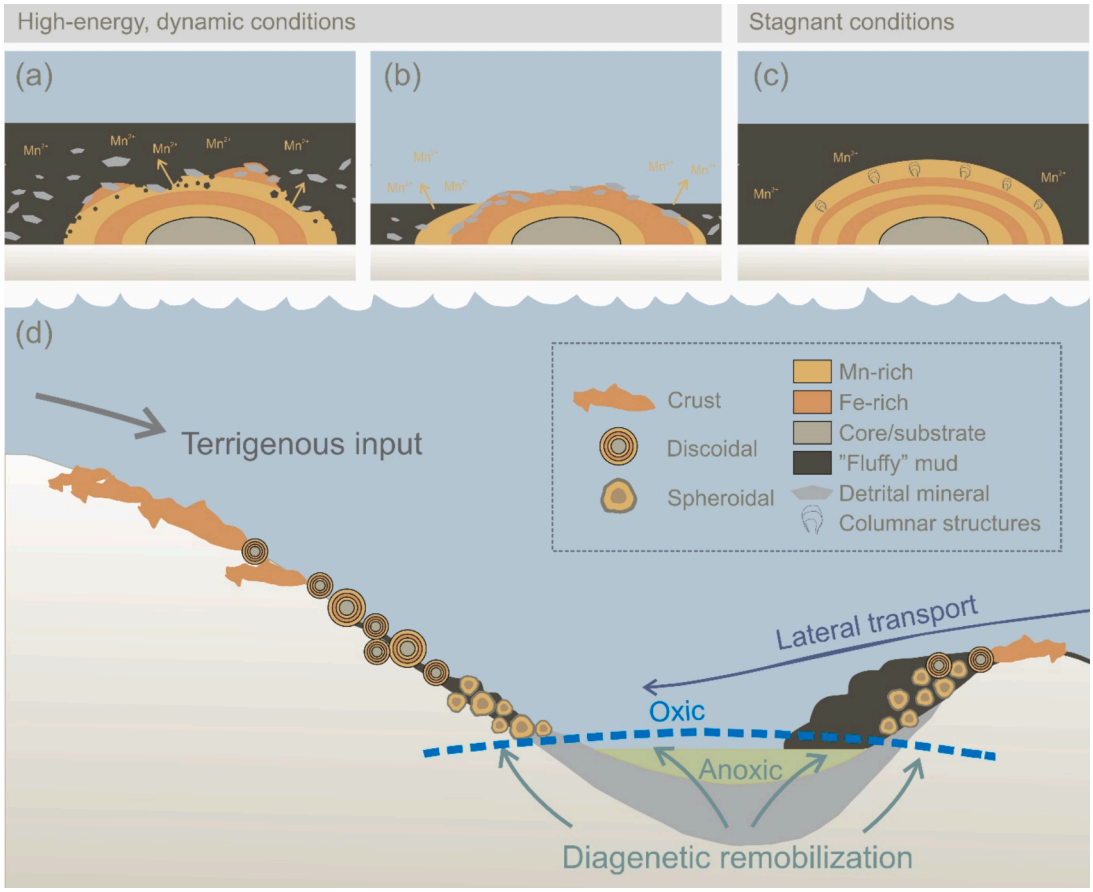

Fig. 15. Schematic model of shelfal ferromanganese concretion formation. At sites with high-energy, dynamic conditions (a and b), the intermittently present fluffy organic-rich mud layer, controlled by near-bottom flows, carries detrital minerals, and influences redox conditions during concretion formation, leading to etching and preferential dissolution of Mn-rich phases (a). Subsequent removal of the fluffy layer enhances Mn transfer to seawater and promotes Fe precipitation (b). In stagnant conditions, the fluffy layer prevents Mn diffusion to seawater and potentially promotes biomineralization of columnar Mn-rich layers. In summary (d), the crust morphotype is usually found in near-shore, relatively high-energy environments, influenced by increased terrigenous input. The spheroidal morphotype is common in deeper water and lower energy setting characterized by lower total detrital mineral content. Discoidal concretions are found in variable formation environments.

hydrodynamic conditions, redox fluctuations, and terrigenous inputs. These factors not only control concretion growth but also have important implications for resource exploration and paleoenvironmental reconstructions, as they influence the concretion composition and geochemical signatures that are preserved over time.

CRediT authorship contribution statement

Joonas Wasiljeff: Writing – review & editing, Writing – original draft, Visualization, Methodology, Investigation, Formal analysis, Data curation, Conceptualization. **Changxun Yu:** Writing – review & editing, Writing – original draft, Visualization, Methodology, Investigation, Formal analysis. **Pasi Heikkilä:** Writing – review & editing, Writing – original draft, Visualization, Methodology, Investigation, Formal analysis. **Yann Lahaye:** Writing – review & editing, Methodology, Investigation, Formal analysis. **Matti Kurhila:** Writing – review & editing, Methodology, Investigation. **Wei-Li Hong:** Writing – review & editing, Resources, Funding acquisition. **Aivo Lepland:** Writing – review & editing, Resources. **Sten Suuroja:** Writing – review & editing, Resources. **Volker Liebetrau:** Resources, Conceptualization. **Joonas J. Virtasalo:** Writing – review & editing, Writing – original draft, Visualization, Supervision, Methodology, Investigation, Funding acquisition, Conceptualization.

Declaration of competing interest

The authors declare that they have no known competing financial interests or personal relationships that could have appeared to influence the work reported in this paper.

Acknowledgments

Two anonymous reviewers are acknowledged for their constructive comments on the manuscript. We thank the crews of r/v *Geomari* and *Electra* for technical assistance. This work was supported by the Research Council of Finland (Fermaid project, grant 332249) and the Swedish Research Council (VR) under the project "Cyrosphere-driven submarine groundwater in the Arctic" (Project No: 2021-04962). This study has used research facilities provided by the Finnish Marine Research Infrastructure (FINMARI) network. We also thank the Canadian Light Source (BioXAS-imaging beamline, 07ID-1) for providing beam time under proposal [39G13872], and Dr. Viorica (Ibi) Bondici for her support and guidance during the experimental session and XRF data analysis.

***Dedication*:** We dedicate this article to Volker Liebetrau, our co-author and collaborator, who passed away on February 7th 2022. Volker is remembered for his enthusiasm, commitment, and smile. This article is only one of the many that carry his memory thanks to his hard work and passion.

Data availability

Data are available through Zenodo at https://doi.org/10.5281/zenodo.13893101.

References

Abbott, A.N., Haley, B.A., McManus, J., 2016. The impact of sedimentary coatings on the diagenetic Nd flux. Earth Planet. Sci. Lett. 449, 217–227.

Anufriev, G.S., Boltenkov, B.S., 2007. Ferromanganese nodules of the Baltic Sea: composition, helium isotopes, and growth rate. Lithol. Miner. Resour. 42, 240–245.

Asikainen, C.A., Werle, S.F., 2007. Accretion of ferromanganese nodules that form pavement in Second Connecticut Lake, New Hampshire. Proc. Natl. Acad. Sci. 104, 17579–17581.

Baturin, G.N., 2019. Distribution of elements in ferromanganese nodules in seas and lakes. Lithol. Miner. Resour. 54, 362–373.

Baturin, G.N., 2010. Element composition of ferromanganese concretions in the Black Sea. Oceanology 50, 83–92.

Baturin, G.N., 2009. Geochemistry of ferromanganese nodules in the Gulf of Finland, Baltic Sea. Lithol. Miner. Resour. 44, 411–426.

Baturin, G.N., Dubinchuk, V.T., 2011. Mineralogy and chemistry of ferromanganese crusts from the Atlantic Ocean. Geochem. Int. 49, 578–593.

Baturin, G.N., Dubinchuk, V.T., 2009. Composition of ferromanganese nodules from Riga Bay (Baltic Sea). Oceanology 49, 111–120.

Bau, M., Koschinsky, A., 2009. Oxidative scavenging of cerium on hydrous Fe oxide: evidence from the distribution of rare earth elements and yttrium between Fe oxides and Mn oxides in hydrogenetic ferromanganese crusts. Geochem. J. 43, 37–47.

Bau, M., Schmidt, K., Koschinsky, A., Hein, J., Kuhn, T., Usui, A., 2014. Discriminating between different genetic types of marine ferro-manganese crusts and nodules based on rare earth elements and yttrium. Chem. Geol. 381, 1–9.

Bertrand, S., Hughen, K.A., Sepúlveda, J., Pantoja, S., 2012. Geochemistry of surface sediments from the fjords of Northern Chilean Patagonia (44–47°S): spatial variability and implications for paleoclimate reconstructions. Geochim. Cosmochim. Acta 76, 125–146.

Biskaborn, B.K., Herzschuh, U., Bolshiyanov, D., Savelieva, L., Diekmann, B., 2012. Environmental variability in northeastern Siberia during the last ~13,300 yr inferred from lake diatoms and sediment–geochemical parameters. Palaeogeogr. Palaeoclimatol. Palaeoecol. 329–330, 22–36.

Blöthe, M., Wegorzewski, A., Müller, C., Simon, F., Kuhn, T., Schippers, A., 2015. Manganese-cycling microbial communities inside deep-sea manganese nodules. Environ. Sci. Technol. 49, 7692–7700.

Callender, E., Bowser, C.J., 1976. Freshwater ferromanganese deposits. In: Wolf, K.H. (Ed.), Au, u, Fe, Mn, Hg, Sb, w, and P Deposits, Handbook of Strata-Bound and Stratiform Ore Deposits. Elsevier, Amsterdam, pp. 341–394.

Couture, R.-M., Hindar, A., Rognerud, S., 2018. Emerging investigator series: geochemistry of trace elements associated with Fe and Mn nodules in the sediment of limed boreal lakes. Environ. Sci. Process. Impacts 20, 406–414.

Cowen, J.P., DeCarlo, E.H., McGee, D.L., 1993. Calcareous nannofossil biostratigraphic dating of a ferromanganese crust from Schumann Seamount. Mar. Geol. 115, 289–306.

Davison, W., 1993. Iron and manganese in lakes. Earth-Sci. Rev. 34, 119–163.

de Souza Machado, A.A., Spencer, K., Kloas, W., Toffolon, M., Zarfl, C., 2016. Metal fate and effects in estuaries: a review and conceptual model for better understanding of toxicity. Sci. Total Environ. 541, 268–281.

Dekov, V.M., Rouxel, O., Guéguen, B., Wegorzewski, A.V., Khripounoff, A., Menot, L., 2021. Mn-micronodules from the sediments of the Clarion-Clipperton zone (Pacific Ocean): origin, elemental source, and Fe-Cu-Zn-isotope composition. Chem. Geol. 580, 120388.

Doucet, L.S., Li, Z.-X., Fougerouse, D., Olierook, H.K.H., Gamaleldien, H., Kirkland, C.L., Hartnady, M.I.H., 2023. The global lead isotope system: toward a new framework reflecting Earth's dynamic evolution. Earth-Sci. Rev. 243, 104483.

Dypvik, H., Harris, N.B., 2001. Geochemical facies analysis of fine-grained siliciclastics using Th/U, Zr/Rb and (Zr+Rb)/Sr ratios. Chem. Geol. 181, 131–146.

Force, E.R., Cannon, W.F., 1988. Depositional model for shallow-marine manganese deposits around Black Shale basins. Econ. Geol. 83, 93–117.

Francke, A., Holtvoeth, J., Codilean, A.T., Lacey, J.H., Bayon, G., Dosseto, A., 2020. Geochemical methods to infer landscape response to Quaternary climate change and land use in depositional archives: a review. Earth-Sci. Rev. 207, 103218.

Frank, M., 2002. Radiogenic isotopes: tracers of past ocean circulation and erosional input. Rev. Geophys. 40, 1-1-1–38.

Frank, M., O'Nions, R.K., Hein, J.R., Banakar, V.K., 1999. 60 Myr records of major elements and Pb–Nd isotopes from hydrogenous ferromanganese crusts: reconstruction of seawater paleochemistry. Geochim. Cosmochim. Acta 63, 1689–1708.

Garzanti, E., Padoan, M., Andò, S., Resentini, A., Vezzoli, G., Lustrino, M., 2013. Weathering and relative durability of detrital minerals in equatorial climate: sand petrology and geochemistry in the East African Rift. J. Geol. 121, 547–580.

Ghiorse, W.C., Hirsch, P., 1982. Isolation and properties of ferromanganese-depositing budding bacteria from Baltic Sea ferromanganese concretions. Appl. Environ. Microbiol. 43, 1464–1472.

Glasby, G.P., 2006. Manganese: predominant role of nodules and crusts. In: Schulz, H.D., Zabel, M. (Eds.), Marine Geochemistry. Springer, Berlin, Heidelberg, pp. 371–427.

Glasby, G.P., 1972. The mineralogy of manganese nodules from a range of marine environments. Mar. Geol. 13, 57–72.

Glasby, G.P., Emelyanov, E.M., Zhamoida, V.A., Baturin, G.N., Leipe, T., Bahlo, R., Bonacker, P., 1997. Environments of formation of ferromanganese concretions in the Baltic Sea: a critical review. Geol. Soc. Lond. Spec. Publ. 119, 213–237.

González, F.J., Somoza, L., Lunar, R., Martínez-Frías, J., Rubí, J.A.M., Torres, T., Ortiz, J. E., Díaz-del-Río, V., 2010. Internal features, mineralogy and geochemistry of ferromanganese nodules from the Gulf of Cadiz: the role of the Mediterranean Outflow Water undercurrent. J. Mar. Syst. 80, 203–218.

Goto, K.T., Nozaki, T., Toyofuku, T., Augustin, A.H., Shimoda, G., Chang, Q., Kimura, J., Kameo, K., Kitazato, H., Suzuki, K., 2017. Paleoceanographic conditions on the São Paulo Ridge, SW Atlantic Ocean, for the past 30 million years inferred from Os and Pb isotopes of a hydrogenous ferromanganese crust. Deep Sea Res. Part II Top. Stud. Oceanogr., Geo- and biodiversity in the South West Atlantic deep sea: the Iatá-piúna expedition with the manned submersible Shinkai 6500 146, 82–92.

Grigoriev, A.G., Zhamoida, V.A., Gruzdov, K.A., Krymsky, R.S., 2013. Age and growth rates of ferromanganese concretions from the Gulf of Finland derived from 210Pb measurements. Oceanology 53, 345–351.

Guan, Y., Ren, Y., Sun, X., Xiao, Z., Wu, Z., Liao, J., Guo, Z., Wang, Y., Huang, Y., 2019. Fine scale study of major and trace elements in the Fe-Mn nodules from the South China Sea and their metallogenic constraints. Mar. Geol. 416, 105978.

Guo, Y., Li, Y., Deng, K., Wang, Z., Yang, S., 2024. Decoding the signals of sediment weathering: toward a quantitative approach. Chem. Geol. 651, 122009.

Halbach, P., Scherhag, C., Hebisch, U., Marchig, V., 1981. Geochemical and mineralogical control of different genetic types of deep-sea nodules from the Pacific Ocean. Miner. Deposita 16, 59–84.

Hayles, S., Al, T., Cornett, J., Harrison, A., Zhao, J., 2021. Growth rates for freshwater ferromanganese concretions indicate regional climate change in eastern Canada at the Northgrippian-Meghalayan boundary. The Holocene 31, 1250–1263.

Heim, C., Quéric, N.-V., Ionescu, D., Schäfer, N., Reitner, J., 2017. Frutexites-like structures formed by iron oxidizing biofilms in the continental subsurface (Äspö Hard Rock Laboratory, Sweden). PLOS ONE 12, e0177542.

Hein, J.R., Konstantinova, N., Mikesell, M., Mizell, K., Fitzsimmons, J.N., Lam, P.J., Jensen, L.T., Xiang, Y., Gartman, A., Cherkashov, G., Hutchinson, D.R., Till, C.P., 2017. Arctic deep water ferromanganese-oxide deposits reflect the unique characteristics of the Arctic Ocean. Geochem. Geophys. Geosystems 18, 3771–3800.

Hein, J.R., Koschinsky, A., 2014. Deep-ocean ferromanganese crusts and nodules. In: Holland, H.D., Turekian, K.K. (Eds.), Treatise on Geochemistry, second ed. Elsevier, Oxford, pp. 273–291.

Hein, J.R., Koschinsky, A., Kuhn, T., 2020. Deep-ocean polymetallic nodules as a resource for critical materials. Nat. Rev. Earth Environ. 1, 158–169.

Hein, J.R., Spinardi, F., Okamoto, N., Mizell, K., Thorburn, D., Tawake, A., 2015. Critical metals in manganese nodules from the Cook Islands EEZ, abundances and distributions. Ore Geol. Rev. 68, 97–116.

Heller, C., Kuhn, T., Versteegh, G.J.M., Wegorzewski, A.V., Kasten, S., 2018. The geochemical behavior of metals during early diagenetic alteration of buried manganese nodules. Deep Sea Res. Part Oceanogr. Res. Pap. 142, 16–33.

Hlawatsch, S., Neumann, T., van den Berg, C.M.G., Kersten, M., Harff, J., Suess, E., 2002. Fast-growing, shallow-water ferro-manganese nodules from the western Baltic Sea: origin and modes of trace element incorporation. Mar. Geol. 182, 373–387.

Huang, S., Fu, Y., 2023. Enrichment characteristics and mechanisms of critical metals in marine Fe-Mn crusts and nodules: a review. Minerals 13, 1532.

Huckriede, H., Meischner, D., 1996. Origin and environment of manganese-rich sediments within black-shale basins. Geochim. Cosmochim. Acta 60, 1399–1413.

Ingri, J., Pontér, C., 1986. Iron and manganese layering in recent sediments in the Gulf of Bothnia. Chem. Geol. 56, 105–116.

Jiang, X.D., Zhao, X., Zhao, X.Y., Chou, Y.-M., Roberts, A.P., Hein, J.R., Yu, J.M., Sun, X. M., Shi, X.F., Cao, W., Liu, Q.S., 2022. Abyssal manganese nodule recording of global cooling and Tibetan Plateau uplift impacts on Asian aridification. Geophys. Res. Lett. 49, e2021GL096624.

Johannesson, K.H., Chevis, D.A., Burdige, D.J., Cable, J.E., Martin, J.B., Roy, M., 2011. Submarine groundwater discharge is an important net source of light and middle REEs to coastal waters of the Indian River Lagoon, Florida, USA. Geochim. Cosmochim. Acta 75, 825–843.

Josso, P., Horstwood, M.S.A., Millar, I.L., Pashley, V., Lusty, P.a.J., Murton, B., 2020a. Development of a correlated Fe-Mn crust stratigraphy using Pb and Nd isotopes and its application to paleoceanographic reconstruction in the Atlantic. Paleoceanogr. Paleoclimatol. 35, e2020PA003928.

Josso, P., Pelleter, E., Pourret, O., Fouquet, Y., Etoubleau, J., Cheron, S., Bollinger, C., 2017. A new discrimination scheme for oceanic ferromanganese deposits using high field strength and rare earth elements. Ore Geol. Rev. 87, 3–15.

Josso, P., Rushton, J., Lusty, P., Matthews, A., Chenery, S., Holwell, D., Kemp, S.J., Murton, B., 2020b. Late Cretaceous and Cenozoic paleoceanography from north-east Atlantic ferromanganese crust microstratigraphy. Mar. Geol. 422, 106122.

Kaikkonen, L., Virtanen, E.A., 2022. Shallow-water mining undermines global sustainability goals. Trends Ecol. Evol. 37, 931–934.

Kaikkonen, L., Virtanen, E.A., Kostamo, K., Lappalainen, J., Kotilainen, A.T., 2019. Extensive coverage of marine mineral concretions revealed in shallow shelf sea areas. Front. Mar. Sci. 6.

Karimian, N., Johnston, S.G., Burton, E.D., 2021. Reductive transformation of birnessite and the mobility of co-associated antimony. J. Hazard. Mater. 404, 124227.

Klemm, V., Levasseur, S., Frank, M., Hein, J.R., Halliday, A.N., 2005. Osmium isotope stratigraphy of a marine ferromanganese crust. Earth Planet. Sci. Lett. 238, 42–48.

Koistinen, T., Stephens, M.B., Bogatchev, V., Nordgulen, Ø., Wennerström, M., Korhonen, J., 2001. Geological map of the fennoscandian shield, scale 1:2 000 000. Geol. Surv. Finl. Nor. Swed. North-West Dep. Nat. Resour. Russ.

Koschinsky, A., Halbach, P., 1995. Sequential leaching of marine ferromanganese precipitates: genetic implications. Geochim. Cosmochim. Acta 59, 5113–5132.

Koschinsky, A., Hein, J.R., 2017. Marine ferromanganese encrustations: archives of changing oceans. Elements 13, 177–182.
Koschinsky, A., Hein, J.R., 2003. Uptake of elements from seawater by ferromanganese crusts: solid-phase associations and seawater speciation. Mar. Geol. 198, 331–351.
Krishnaswami, S., Moore, W.S., 1973. Accretion rates of freshwater manganese deposits. Nat. Phys. Sci. 243, 114–116.
Ksenia, P., Andrzej, S., Beldowski, J., Emeis, K., Thomas, L., Pempkowiak, J., 2001. Variations in organic matter bound in fluffy layer suspended matter from the Pomeranian Bay (Baltic Sea). Oceanologia 43.
Kuosa, H., Fleming-Lehtinen, V., Lehtinen, S., Lehtiniemi, M., Nygård, H., Raateoja, M., Raitaniemi, J., Tuimala, J., Uusitalo, L., Suikkanen, S., 2017. A retrospective view of the development of the Gulf of Bothnia ecosystem. J. Mar. Syst. 167, 78–92.
Kylander, M., Klaminder, J., Wohlfarth, B., Löwemark, L., 2013. Geochemical responses to paleoclimatic changes in southern Sweden since the late glacial: the Hässeldala Port lake sediment record. J. Paleolimnol. 50.
Leipe, T., Tauber, F., Vallius, H., Virtasalo, J., Uścinowicz, S., Kowalski, N., Hille, S., Lindgren, S., Myllyvirta, T., 2011. Particulate organic carbon (POC) in surface sediments of the Baltic Sea. Geo-Mar. Lett. 31, 175–188.
Lenz, C., Jilbert, T., Conley, D.J., Slomp, C.P., 2015. Hypoxia-driven variations in iron and manganese shuttling in the Baltic Sea over the past 8 kyr. Geochem. Geophys. Geosyst. 16, 3754–3766.
Li, Y., Zhao, X., Wu, J., Gu, X., 2020. Surface complexation modeling of divalent metal cation adsorption on birnessite. Chem. Geol. 551, 119774.
Liebetrau, V., Eisenhauer, A., Frei, R., Kronz, A.B.B., Hansen, B.T.L., 2004. Radiometric growth rate and Pb isotope evolution of Mn/Fe precipitates from the SW-Baltic Sea. Z. Für Angew. Geol. 2, 195–215.
Liebetrau, V., Eisenhauer, A., Gussone, N., Wörner, G., Hansen, B.T., Leipe, T., 2002. 226Raexcess/Ba growth rates and U-Th-Ra-Ba systematic of Baltic Mn/Fe crusts. Geochim. Cosmochim. Acta 66, 73–83.
Ling, H.-F., Jiang, S.-Y., Frank, M., Zhou, H.-Y., Zhou, F., Lu, Z.-L., Chen, X.-M., Jiang, Y.-H., Ge, C.-D., 2005. Differing controls over the Cenozoic Pb and Nd isotope evolution of deepwater in the central North Pacific Ocean. Earth Planet. Sci. Lett. 232, 345–361.
Lintunen, K., Kasvi, E., Uvo, C.B., Alho, P., 2024. Changes in the discharge regime of Finnish rivers. J. Hydrol. Reg. Stud. 53, 101749.
Liu, L., Jiang, G., Mao, X., Zhao, H., Zhao, Y., Li, Y., Zhao, H.a., Bi, Z., 2022. Geochemical composition of surface sediments in the Bashang area, North China and its environmental significance. Front. Earth Sci. 10.
Löffler, A., Leipe, T., Emeis, K.-C., 2000. The fluffy layer in the Pomeranian Bight (western Baltic Sea): geochemnistry, mineralogy and enviromental aspects. MEYNIANA 52, 85–100.
Luo, Y., Li, S., Tan, W., Qiu, G., Liu, F., Cai, C., 2017. Oxidation and catalytic oxidation of dissolved sulfide by manganite in aqueous systems. Clays Clay Miner. 65, 299–309.
Lüthgens, C., Hardt, J., Böse, M., 2020. Proposing a new conceptual model for the reconstruction of ice dynamics in the SW sector of the Scandinavian Ice Sheet (SIS) based on the reinterpretation of published data and new evidence from optically stimulated luminescence (OSL) dating. EG Quat. Sci. J. 69, 201–223.
Majamäki, R., Wasiljeff, J., Purkamo, L., Hultman, J., Asmala, E., Yli-Hemminki, P., Jørgensen, K.S., Koho, K., Kuva, J., Virtasalo, J.J., 2025. Microbially-enhanced growth and metal capture by ferromanganese concretions in a laboratory experiment. Geobiology 23, e70010.
Manceau, A., Lanson, M., Takahashi, Y., 2014. Mineralogy and crystal chemistry of Mn, Fe, Co, Ni, and Cu in a deep-sea Pacific polymetallic nodule. Am. Mineral. 99, 2068–2083.
Marcus, M.A., Edwards, K.J., Gueguen, B., Fakra, S.C., Horn, G., Jelinski, N.A., Rouxel, O., Sorensen, J., Toner, B.M., 2015. Iron mineral structure, reactivity, and isotopic composition in a South Pacific Gyre ferromanganese nodule over 4Ma. Geochim. Cosmochim. Acta 171, 61–79.
Marcus, M.A., Manceau, A., Kersten, M., 2004. Mn, Fe, Zn and As speciation in a fast-growing ferromanganese marine nodule. Geochim. Cosmochim. Acta 68, 3125–3136.
Mayanna, S., Peacock, C.L., Schäffner, F., Grawunder, A., Merten, D., Kothe, E., Büchel, G., 2015. Biogenic precipitation of manganese oxides and enrichment of heavy metals at acidic soil pH. Chem. Geol. 402, 6–17.
Moore, W.S., Dean, W.E., Krishnaswami, S., Borole, D.V., 1980. Growth rates of manganese nodules in Oneida Lake, New York. Earth Planet. Sci. Lett. 46, 191–200.
Müller, P.J., Hartmann, M., Suess, E., 1988. The chemical environment of pelagic sediments. In: Halbach, P., Friedrich, G., von Stackelberg, U. (Eds.), The manganese nodule belt of the Pacific Ocean. Geological environment, nodule formation, and mining aspects. Ferdinand Enke Verlag, Stuttgart. pp. 70–90.
Neff, J.M., 2002. Chapter 10 – zinc in the ocean. In: Neff, J.M. (Ed.), Bioaccumulation in Marine Organisms. Elsevier, Oxford, pp. 175–189.
Nesbitt, H.W., Young, G.M., 1982. Early Proterozoic climates and plate motions inferred from major element chemistry of lutites. Nature 299, 715–717.
Park, J., Jung, J., Ko, Y., Lee, Y., Yang, K., 2023. Reconstruction of the paleo-ocean environment using mineralogical and geochemical analyses of mixed-type ferromanganese nodules from the tabletop of Western Pacific Magellan Seamount. Geochem. Geophys. Geosystems 24, e2022GC010768.
Parker, A., 1970. An index of weathering for silicate rocks. Geol. Mag. 107, 501–504.
Pempkowiak, J., Beldowski, J., Pazdro, K., Staniszewski, A., Zaborska, A., Leipe, T., Emeis, K., 2005. Factors influencing fluffy layer suspended matter (FLSM) properties in the Odra River – Pomeranian Bay – Arkona Deep System (Baltic Sea) as derived by principal components analysis (PCA), and cluster analysis (CA). Hydrol. Earth Syst. Sci. 9, 67–80.
Post, J.E., 1999. Manganese oxide minerals: crystal structures and economic and environmental significance. Proc. Natl. Acad. Sci. 96, 3447–3454.
Pourmand, A., Dauphas, N., Ireland, T.J., 2012. A novel extraction chromatography and MC-ICP-MS technique for rapid analysis of REE, Sc and Y: revising CI-chondrite and Post-Archean Australian Shale (PAAS) abundances. Chem. Geol. 291, 38–54.
Qiao, Q., Yang, X., Liu, L., Luo, Y., Tan, W., Liu, C., Dang, Z., Qiu, G., 2020. Electrochemical adsorption of cadmium and arsenic by natural Fe-Mn nodules. J. Hazard. Mater. 390, 122165.
Ravel, B., Newville, M., 2005. ATHENA, ARTEMIS, HEPHAESTUS: data analysis for X-ray absorption spectroscopy using IFEFFIT. J. Synchrotron Radiat. 12, 537–541.
Reimann, C., Birke, M., Demetriades, A., Filzmoser, P., O'Connor, P., 2014a. Chemistry of Europe's Agricultural Soils, Part A. Schweizerbart'sche Verlagsbuchhandlung. Hannover.
Reimann, C., Birke, M., Demetriades, A., Filzmoser, P., O'Connor, P., 2014b. Chemistry of Europe's Agricultural Soils, Part B. Schweizerbart'sche Verlagsbuchhandlung. Hannover.
Reimann, C., Flem, B., Fabian, K., Birke, M., Ladenberger, A., Négrel, P., Demetriades, A., Hoogewerff, J., 2012. Lead and lead isotopes in agricultural soils of Europe – the continental perspective. Appl. Geochem. 27, 532–542.
Ren, J., He, G., Deng, X., Deng, X., Yang, Y., Yao, H., Yang, S., 2022. Metallogenesis of Co-rich ferromanganese nodules in the northwestern Pacific: selective enrichment of metallic elements from seawater. Ore Geol. Rev. 143, 104778.
Ren, J., He, G., Yang, Y., Yu, M., Deng, Y., Pang, Y., Zhao, B., Yao, H., 2024a. Ultraselective enrichment of trace elements in seawater by Co-rich ferromanganese nodules. Glob. Planet. Change 239, 104498.
Ren, J., Yang, Y., Yu, M., Liu, J., Luo, S., Li, J., Deng, X., Zhang, X., Dong, F., Zhang, L., Wei, Z., He, G., 2024b. Spatial distribution of critical metals and chemostratigraphy in Co-rich ferromanganese nodules in the northwestern Pacific Ocean. J. Geophys. Res. Oceans 129, e2024JC021287.
Ren, Y., Guan, Y., Sun, X., Xu, L., Xiao, Z., Deng, Y., He, W., 2023. Nano-mineralogy and growth environment of Fe-Mn polymetallic crusts and nodules from the South China Sea. Front. Mar. Sci. 10.
Reunamo, A., Yli-Hemminki, P., Nuutinen, J., Lehtoranta, J., Jørgensen, K.S., 2017. Degradation of crude oil and PAHs in iron–manganese concretions and sediment from the northern Baltic Sea. Geomicrobiol. J. 34, 385–399.
Saarnisto, M., Saarinen, T., 2001. Deglaciation chronology of the Scandinavian Ice Sheet from the Lake Onega Basin to the Salpausselkä End Moraines. Glob. Planet. Change, The late Quaternary stratigraphy and environments of northern Eurasia and the adjacent Arctic seas - new contributions from QUEEN 31, 387–405.
Sangster, D.F., Outridge, P.M., Davis, W.J., 2000. Stable lead isotope characteristics of lead ore deposits of environmental significance. Environ. Rev. 8, 115–147.
Sauramo, M., 1929. The quaternary geology of Finland. Bull. Comm. Géologique Finl. 86, 1–110.
Scarlett, N.V.Y., Madsen, I.C., 2006. Quantification of phases with partial or no known crystal structures. Powder Diffr. 21, 278–284.
Schmidt, K., Bau, M., Hein, J.R., Koschinsky, A., 2014. Fractionation of the geochemical twins Zr–Hf and Nb–Ta during scavenging from seawater by hydrogenetic ferromanganese crusts. Geochim. Cosmochim. Acta 140, 468–487.
Scopelliti, G., Russo, V., 2021. Petrographic and geochemical characterization of the Middle–Upper Jurassic Fe–Mn crusts and mineralizations from Monte Inici (north-western Sicily): genetic implications. Int. J. Earth Sci. 110, 559–582.
Shulga, N., Abramov, S., Klyukina, A., Ryazantsev, K., Gavrilov, S., 2022. Fast-growing Arctic Fe–Mn deposits from the Kara Sea as the refuges for cosmopolitan marine microorganisms. Sci. Rep. 12, 21967.
Sjöberg, S., Callac, N., Allard, B., Smittenberg, R.H., Dupraz, C., 2018. Microbial communities inhabiting a rare earth element enriched birnessite-type manganese deposit in the Ytterby mine, Sweden. Geomicrobiol. J. 35, 657–674.
Sjöberg, S., Yu, C., Stairs, C.W., Allard, B., Hallberg, R., Henriksson, S., Åström, M., Dupraz, C., 2021. Microbe-mediated Mn oxidation—a proposed model of mineral formation. Minerals 11, 1146.
Solé, V.A., Papillon, E., Cotte, M., Walter, Ph., Susini, J., 2007. A multiplatform code for the analysis of energy-dispersive X-ray fluorescence spectra. Spectrochim. Acta Part B at. Spectrosc. 62, 63–68.
Stratmann, T., Soetaert, K., Kersken, D., van Oevelen, D., 2021. Polymetallic nodules are essential for food-web integrity of a prospective deep-seabed mining area in Pacific abyssal plains. Sci. Rep. 11, 12238.
Stroeven, A.P., Hättestrand, C., Kleman, J., Heyman, J., Fabel, D., Fredin, O., Goodfellow, B.W., Harbor, J.M., Jansen, J.D., Olsen, L., Caffee, M.W., Fink, D., Lundqvist, J., Rosqvist, G.C., Strömberg, B., Jansson, K.N., 2016. Deglaciation of Fennoscandia. Quat. Sci. Rev., Special Issue: PAST Gateways (palaeo-Arctic Spatial and Temporal Gateways) 147, 91–121.
Stumm, W., Morgan, J.J., 1996. Aquatic Chemistry: Chemical Equilibria and Rates in Natural Waters, third ed. Wiley.
Sujith, P.P., Gonsalves, M.J.B.D., 2021. Ferromanganese oxide deposits: geochemical and microbiological perspectives of interactions of cobalt and nickel. Ore Geol. Rev. 139, 104458.
Sutherland, K.M., Wankel, S.D., Hein, J.R., Hansel, C.M., 2020. Spectroscopic insights into ferromanganese crust formation and diagenesis. Geochem. Geophys. Geosyst. 21, e2020GC009074.
Sweetman, A.K., Smith, A.J., de Jonge, D.S.W., Hahn, T., Schroedl, P., Silverstein, M., Andrade, C., Edwards, R.L., Lough, A.J.M., Woulds, C., Homoky, W.B., Koschinsky, A., Fuchs, S., Kuhn, T., Geiger, F., Marlow, J.J., 2024. Evidence of dark oxygen production at the abyssal seafloor. Nat. Geosci. 17, 737–739.
Takahashi, Y., Manceau, A., Geoffroy, N., Marcus, M.A., Usui, A., 2007. Chemical and structural control of the partitioning of Co, Ce, and Pb in marine ferromanganese oxides. Geochim. Cosmochim. Acta 71, 984–1008.

Tani, Y., Kakinuma, S., Chang, J., Tanaka, K., Miyata, N., 2021. Preferential elimination of Ba2+ through irreversible biogenic manganese oxide sequestration. Minerals 11, 53.
Tebo, B., Bargar, J., Clement, B., Dick, G., Murray, K., Parker, D., Verity, R., Webb, S., 2004. Biogenic manganese oxides: properties and mechanisms of formation. Apr. Annu. Rev. Earth Planet. Sci. 21, 287–328.
Tessier, A., Fortin, D., Belzile, N., DeVitre, R.R., Leppard, G.G., 1996. Metal sorption to diagenetic iron and manganese oxyhydroxides and associated organic matter: narrowing the gap between field and laboratory measurements. Geochim. Cosmochim. Acta 60, 387–404.
Thierry, S., Dick, S., George, S., Benoit, L., Cyrille, P., 2019. EMODnet Bathymetry a compilation of bathymetric data in the European waters. In: OCEANS 2019—Marseille. Presented at the OCEANS 2019—Marseille, pp. 1–7.
Tomczyk, C., 2022. A database of lead isotopic signatures of copper and lead ores for Europe and the Near East. J. Archaeol. Sci. 146, 105657.
Usui, A., Mellin, T.A., Nohara, M., Yuasa, M., 1989. Structural stability of marine 10 Å manganates from the Ogasawara (Bonin) Arc: implication for low-temperature hydrothermal activity. Mar. Geol. 86, 41–56.
Vereshchagin, O.S., Perova, E.N., Brusnitsyn, A.I., Ershova, V.B., Khudoley, A.K., Shilovskikh, V.V., Molchanova, E.V., 2019. Ferro-manganese nodules from the Kara Sea: mineralogy, geochemistry and genesis. Ore Geol. Rev. 106, 192–204.
Verlaan, P.A., Cronan, D.S., 2022. Origin and variability of resource-grade marine ferromanganese nodules and crusts in the Pacific Ocean: a review of biogeochemical and physical controls. Geochemistry 82, 125741.
Verstijnen, Y.J.M., Lucassen, E.C.H.E.T., Wagenvoort, A.J., Ketelaars, H.A.M., van der Velde, G., Smolders, A.J.P., 2024. Trophic Transfer of Cd, Cu, Pb, Zn, P and Se in Dutch Storage Water Reservoirs. Arch. Environ. Contam. Toxicol. 86, 217–233.
Virtasalo, J.J., Hämäläinen, J., Kotilainen, A.T., 2014. Toward a standard stratigraphical classification practice for the Baltic Sea sediments: the CUAL approach. Boreas 43, 924–938.
Virtasalo, J.J., Kotilainen, A.T., 2008. Phosphorus forms and reactive iron in lateglacial, postglacial and brackish-water sediments of the Archipelago Sea, northern Baltic Sea. Mar. Geol. 252, 1–12.
Virtasalo, J.J., Kotilainen, A.T., Räsänen, M.E., Ojala, A.E.K., 2007. Late-glacial and post-glacial deposition in a large, low relief, epicontinental basin: the northern Baltic Sea. Sedimentology 54, 1323–1344.
Wasiljeff, J., Salminen, J.M., Roberts, A.P., Hu, P., Brown, M., Kuva, J., Lukkari, S., Jolis, E.M., Heinsalu, A., Hong, W.-L., Lepland, A., Suuroja, S., Parkkonen, J., Virtasalo, J.J., 2024a. Morphology-dependent magnetic properties in shallow-water ferromanganese concretions. Geochem. Geophys. Geosystems 25, e2023GC011366.
Wasiljeff, J., Yu, C., Heikkilä, P., Lahaye, Y., Kurhila, M., Hong, W.-L., Lepland, A., Suuroja, S., Liebetrau, V., Virtasalo, J.J., 2024b. Mineral phases and growth conditions of morphologically diverse shelfal ferromanganese concretions. Zenodo.
Webb, S.M., 2005. Structural characterization of biogenic Mn oxides produced in seawater by the marine bacillus sp. strain SG-1. Am. Mineral. 90, 1342–1357.
Wegorzewski, A.V., Kuhn, T., 2014. The influence of suboxic diagenesis on the formation of manganese nodules in the Clarion Clipperton nodule belt of the Pacific Ocean. Mar. Geol. 357, 123–138.
Williams, T.M., Owen, R.B., 1992. Geochemistry and origins of lacustrine ferromanganese nodules from the Malawi Rift. Central Africa. Geochim. Cosmochim. Acta 56, 2703–2712.
Winterhalter, B., 2004. Ferromanganese concretions in the Gulf of Bothnia. In: Harff, J., Emelyanov, E., Schmidt-Tome, M., Spiridonov, M. (Eds.), Mineral Resources of the Baltic Sea – Exploration, Exploitation and Sustainable Development. Zeitschrift Fur Angewandte Geologie.
Winterhalter, B., 1980. Ferromanganese concretions in the Gulf of Bothnia. In: Varentsov, I.M., Graselly, G. (Eds.), Geology and Geochemistry of Manganese III. Hungarian Academy of Sciences, Budapest, pp. 227–254.
Yli-Hemminki, P., Jørgensen, K.S., Lehtoranta, J., 2014. Iron–manganese concretions sustaining microbial life in the Baltic Sea: the structure of the bacterial community and enrichments in metal-oxidizing conditions. Geomicrobiol. J. 31, 263–275.
Zhamoida, V., Grigoriev, A., Gruzdov, K., Ryabchuk, D., 2007. The influence of ferromanganese concretions-forming processes in the Eastern Gulf of Finland on the marine environment. Spec. Pap. - Geol. Surv. Finl. 45, 21–32.
Zhamoida, V., Grigoriev, A., Ryabchuk, D., Evdokimenko, A., Kotilainen, A.T., Vallius, H., Kaskela, A.M., 2017. Ferromanganese concretions of the eastern Gulf of Finland – environmental role and effects of submarine mining. J. Mar. Syst. 172, 178–187.
Zhamoida, V.A., Butylin, W.P., Glasby, G.P., Popova, I.A., 1996. The nature of ferromanganese concretions from the eastern Gulf of Finland, Baltic Sea. Mar. Georesources Geotechnol. 14, 161–176.
Zhang, F.S., Lin, C.Y., Bian, L.Z., Glasby, G.P., Zhamoida, V., 2002. Possible evidence for the biogenic formation of spheroidal ferromanganese concretions from the eastern Gulf of Finland, the Baltic Sea. Baltica 15, 23–29.
Zhang, H., Cui, Y., Zong, S., Chen, S., Ma, L., Wang, W., Wang, X., Li, S., Liu, C., 2025. Origin and critical metals enrichment of ferromanganese precipitates from Jiawang Seamount (Hook Ridge) Antarctica: geochemistry and isotope evidence. Mar. Geol. 479, 107435.
Zhong, Y., Chen, Z., González, F.J., Hein, J.R., Zheng, X., Li, G., Luo, Y., Mo, A., Tian, Y., Wang, S., 2017. Composition and genesis of ferromanganese deposits from the northern South China Sea. J. Asian Earth Sci. 138, 110–128.